

EXPERIMENTAL INVESTIGATIONS OF SOLID STATE STEEL ENERGY ABSORBERS
FOR EARTHQUAKE RESISTANT STRUCTURES

by

FOO-LIN CHOW

A THESIS SUBMITTED IN PARTIAL FULFILMENT OF THE
REQUIREMENTS FOR THE DEGREE OF
MASTER OF APPLIED SCIENCE

in

THE FACULTY OF GRADUATE STUDIES
(The Department of Civil Engineering)

We accept this thesis as conforming
to the required standard

THE UNIVERSITY OF BRITISH COLUMBIA

November 1983

© Foo-Lin Chow, 1983

In presenting this thesis in partial fulfilment of the requirements for an advanced degree at the University of British Columbia, I agree that the Library shall make it freely available for reference and study. I further agree that permission for extensive copying of this thesis for scholarly purposes may be granted by the Head of my Department or by his representatives. It is understood that copying or publication of this thesis for financial gain shall not be allowed without my written permission.

Department of Civil Engineering

The University of British Columbia

2324 Main Mall

Vancouver, B.C.

V6T 1W5

Canada

Date: 18. Nov. 1983 .

ABSTRACT

This thesis suggests the use of curved plates and bars of hot rolled mild steel as energy dissipating devices for the design of earthquake-resistant structures. The proposed devices would be used in parallel with isolating systems in buildings or other structures. They are designed to deflect elastically under minor loads such as wind and to deform plastically when subjected to major earthquake loadings. The devices have a large energy absorbing capacity at a high number of cycles; they are economical and, once installed, can be easily inspected and replaced. An engineering method is presented for predicting the number of cycles to failure of the devices. The practical application and feasibility of a base-isolated steel structure with discrete yield rings is demonstrated in a model test on a shaking table. A design method for the yield rings is proposed.

TABLE OF CONTENTS

	<u>Page</u>
ABSTRACT	-i-
LIST OF TABLES	-iii-
LIST OF FIGURES	-iv-
ACKNOWLEDGEMENTS	-vi-
1. INTRODUCTION	1
2. X-SHAPED ENERGY ABSORBER	3
2.1. Description of Function	3
2.2. Experimental Investigations and Results	4
2.3. Analysis and Design	7
3. YIELD RING	9
3.1. Description of Function	9
3.2. Experimental Investigations and Results	9
3.3. Analysis and Design	11
4. IMPLEMENTATION OF YIELD RINGS	15
4.1. Description and Experimental Set-Up	15
4.2. Analytical Modeling	16
4.3. Test Results and Proposal for Yield Ring Design	21
5. CONCLUSIONS	27
6. REFERENCES	29
7. TABLES	32
8. FIGURES	41

LIST OF TABLES

	<u>Page</u>
Table 1: Dimensions of X-Shaped Energy Absorber	32
Table 2: Low Cycle Fatigue Test Results	33
Table 3: Theoretical and Experimental Values of Strain for X-Shaped Energy Absorber	34
Table 4: Theoretical and Experimental Values of Strain for Yield Ring	34
Table 5: Dimension of Yield Rings Used in Low Cycle Fatigue Tests.	35
Table 6: Stiffness, Yield Force and Natural Frequencies for Different Yield Ring Combinations.	35
Table 7: Peak Values for Accelerations and Displacement of Sinusoidal Table Excitation Used for Tests	36
Table 8: Peak Values for Accelerations and Displacements of Earthquake Table Excitation Used for Tests	36
Table 9: Displacement Ratios for Different Frequencies of Sinusoidal Excitation and Different Yield Rings.	37
Table 10: Acceleration Response Attenuation Ratios for Different Sinusoidal Excitations	38
Table 11: Acceleration Response Attenuation Ratios for Different Earthquake Excitations	39
Table 12: Modified Mercally Intensity Scale.	40
Table 13: Predominant Frequencies for Different Soil Conditions.	40

LIST OF FIGURES

	<u>Page</u>
Fig. 1: X-Shaped Energy Absorber	41
Fig. 2: Load-Displacement Hysteresis Loops for X-Shaped Energy Absorber and Yield Ring	41
Fig. 3: Test Set-Up Low Cycle Fatigue Tests.	42
Fig. 4: X-Shaped Energy Absorbers.	42
Fig. 5: Strain Gauges Applied to Energy Absorber	43
Fig. 6: Locations of Strain Gauges	43
Fig. 7: Test Results of Relation of Strain and Cycle to Failure.	44
Fig. 8: Characteristic Values and Hysteresis Loop of Energy Absorber	45
Fig. 9: Microcrack Development in Low Cycle Fatigue Test . . .	45
Fig. 10: Hysteresis Loop for Biased Energy Absorber	46
Fig. 11: Anticlastic Bending of Energy Absorber	47
Fig. 12: Strain-Displacement Relation for Energy Absorber . . .	48
Fig. 13: Quarter Component of Double Yield Ring	49
Fig. 14: Geometric Deformation of Yield Ring.	49
Fig. 15: Fractured Yield Ring	50
Fig. 16: Displaced Yield Ring	50
Fig. 17: Twisted Yield Ring	51
Fig. 18: Yield Ring with Applied Strain Gauges.	51
Fig. 19: Locations of Strain Gauges on Yield Ring	52
Fig. 20: Displacement of Yield Ring in Y-Direction.	52
Fig. 21: Displacement of Yield Ring in Z-Direction.	53

Fig. 22:	Strain-Displacement Relation of Yield Ring	53
Fig. 23:	Components of Base Isolation Model /7/	54
Fig. 24:	Roller Element /18/	54
Fig. 25:	Base-Isolation System With Two Quarter Yield Rings . .	55
Fig. 26:	Base-Isolation System With One Quarter Yield Ring. . .	55
Fig. 27:	Structure and Model With Base-Isolation and Yield Ring	56
Fig. 28:	Load Displacement Hysteresis Loop for Yield Ring . . .	56
Fig. 29:	Displacement Magnification Factor for Different Attenuation Ratios	57
Fig. 30:	Relation of Damping and Ductility Factor	58
Fig. 31:	Attenuation Ratio Over Frequency Ratio for Sinusoidal Excitation	59
Fig. 32:	Attenuation Ratio Over Frequency Ratio for Earthquake Excitation	59
Fig. 33:	X-Shaped Energy Absorber Implemented in Flexible Spatial Piping System, Schematic from /4/.	60
Fig. 34:	Yield Rings Implemented in Base Isolation System, From /7/, Insert: Proposal for Bi-Directional Use /18/. .	60

ACKNOWLEDGEMENTS

The author wishes to thank the staff of the Civil Engineering Department who have contributed to the success of this project. In particular, I thank Dr. J.P. Duncan, who provided most of the test specimens from his numerically controlled mill, and Bernard Merkle and Max Nazar, who supported me in the experimental set-ups and conduction of tests. I would like to thank the technical staff in the workshop of the Department of Civil Engineering with Richard Postgate as its supervisory technician and Wolfram Schmitt from the Electronic Laboratory.

Very helpful in discussions was my colleague student Bill Lipsett and during conducting the shaking table tests Bill Barwig, who repeatedly stressed our supervisor's patience by his frequent presence in the laboratory, and the table operator Chris Dumont.

I am infinitely grateful to my parents, who supported me here in Vancouver and to my wife, who is still waiting for my return in my mother country. Great acknowledgements I would like to express to the People's Republic of China for giving me the opportunity for further education in Canada. I also would like to thank all my Canadian friends, whose friendship I have enjoyed very much during my stay in Canada.

I thank my supervisor Dr. S.F. Stiemer for his help and guidance during my graduate studies and these investigations, which were made possible by the funding provided by the Natural Sciences and Engineering Research Council of Canada, Grant No. A 1840.

CHAPTER 1

INTRODUCTION

Earthquake resistant design in structural engineering is achieved by several methods of which the following have recently received the highest interest: 1) sufficiently stiffening the buildings and internally absorbing the earthquake forces by inelastic action in beams or columns or, 2), designing a very flexible elastic structure and externally absorbing the energy by additional discrete elements or, 3), uncoupling the building or structure from the exciting ground motion and restricting it from excessive displacements by dampers. The latter approach has been readily accepted in theory but it has been viewed as impractical for large civil engineering structures. The lack of acceptance of this method has been caused in part by its complete contrast to the current approach to aseismic design described under 1). This method requires that the structure has to be analysed non-linear elastically, which usually is not only difficult but costly. During an earthquake large yielding deformations and cracking occur, and although without total destruction the structure will become either useless or will require expensive repair. Many different design proposals were introduced and implemented in prototypes, while the most recent ones (asymmetric bracing, sacrificial shear walls, etc.) were trying to pre-determine the location of yielding and fracture and thus simplifying analysis, design and repair. Structures designed using methods 2) or 3) do not withstand earthquake loadings by the structure's strength or by sacrificing parts of the structure but limit the forces in the

structure by elasticity or by uncoupling it from the ground. However, if a structure designed by the elastic system, 2), does not include damping devices, there is the obvious danger of it developing resonances during excitation which would cause failure. With a proper design which includes discrete damping devices this problem can be prevented. When a building is isolated from the ground motion, which is a relatively old but seldom used system, measures must be undertaken to prevent the relative displacements versus the ground during a severe earthquake from becoming so large and that minor loads could permanently displace the building.

CHAPTER 2

X-SHAPED ENERGY ABSORBER2.1. Description of Function

The investigations were aimed at the design of reliable, inexpensive solid-state energy absorbers for a) a mono-axial action and b) a multi-directional action.

After considering a large variety of shapes and using results from previous research [1] - [5] a bending element was chosen for further development. Based on successful experiments in [3] and [4] bending action promised a yield element which is easier to manufacture but possesses similar reserve capacity like a torsion element. All shear, compression, tension, and extrusion action apparently inherited major disadvantages. They were excluded from further design considerations. Simple hot rolled steel plates were used for the yield elements. Complicated machining or welding were avoided. No hinged bearings were required, the devices were rigidly clamped (rotationally fixed) at both ends.

For the one-directional type a shape was chosen, which was composed from double tapers forming an X. To avoid stress concentrations at the clamped boundaries or in the middle, rounded transitions were chosen (Fig. 1). When this flat plate of mild steel was loaded in the weak direction, the fixed bending stresses at the apex of the tapers became uniform along the length, thus allowing yielding to develop over the full length of both tapered sections. The plate deformed in a continuous S-shape. This assured an optimum use of the

existing material without stress concentrations at any location of the device and resulted in a high number of cycles far into the ductile range of the material. Because there was always a residual elastic core inside the yielding plate, the energy absorber achieved self-centering after being subjected to random load time-histories with decaying ends, which is a very beneficial behaviour in the case of earthquake loads. Although the fatigue life, work hardening characteristics, and amount of energy absorption varied from steel to steel quality, even from batch to batch, the St 10-20 hot rolled mild steel showed a rather uniform behaviour (Fig. 2).

2.2. Experimental Investigations and Results

A large number of specimens (see Table 1) were tested in order to get reliable results for the yielding region and the fatigue life of the devices. Any length, thickness or width effects due to grain sizes or shape effects were tried to be covered. Investigations [9] and [10] on low cycle fatigue for mild steel indicated, that the number of cycles depended mainly on the absolute maximum strain under cyclic loading.

All test specimens were machined by a numerically controlled mill, thus achieving highest accuracy of the geometric shape. The steel plates were made from St 10-20 hot-rolled mild steel, which is commercially available in many different widths and thicknesses. One end of the plates was rigidly clamped to the base beam of the test rig, while the other was connected to a rod and a hydraulically actuated piston (see Fig. 3 and Fig. 4). The hydraulic system could be force- or displacement-controlled by an MTS-system Model 904.5 S. During most of

the tests, the displacement control was used. The cycle frequency was kept so low, that the plates did not heat up considerably (not more than 100°C). If the temperature is not increased too much, the frequency has no significant effects on the final number of cycles to failure. I mostly used for one period one second. Tests were conducted using strain gauges to measure the strain distribution on the surface of the specimen (see Figs. 5 and 6). The strain gauges were placed on each side of the plate. A high precision, computer-controlled strain and voltage data acquisition and analysis system (OPTILOG and Apple II) monitored displacements, forces, and deformations during the tests. It was possible to store all data on magnetic disks for future display and discussion.

The locations #3 and #4 (see Fig. 6) showed slightly higher strain levels than #2. For location #1 very small strains were measured, which was close to the theoretically expected value (no strain for an ideally centered strain gauge at midspan).

Failure occurred in all cases close to the clamped boundaries, approximately at locations #3 and #4. The dimensions of the test specimens and the number of cycles to failure are listed in Table 2 and plotted in Fig. 7. A simulated thermal bias, which resulted in a shift of the zero position in the unloaded situation, reduced the maximum number of cycles, when compared with an unbiased energy absorber.

The idealized deflected shape of the energy absorber is shown in Fig. 8. During one full displacement cycle of $\pm d$ the load-displacement curve describes a hysteretic loop. The area inside this loop represents the absorbed energy per cycle. This hysteretic loop was stable from approx. cycle number 3 to failure minus 10-20%. During

the first three cycles, the loop gradually grew to the stable shape, which then remained its shape until shortly before failure. Failure did not occur without warning. Microcracks in the expected area of fracture could be observed at the same instant when the hysteresis loop lowered its yield level. Although ordinary steel flats were used without special selection, the microcrack pattern was always nicely symmetrical and very regular (see Fig. 9). When the simulated thermal bias was applied after the stable hysteresis loop had developed (after 50, 100, 150 cycles), a new stable loop shape formed subsequently in three cycles. This new stable shape was slightly unsymmetrical due to geometrical effects in the deflected S-shape. When the energy absorber was bent in the direction of the applied bias, some force was already applied in tension in the element, which showed up in the diagram as a deformation of the yield plateau (see Fig. 10). Another interesting effect could be observed: when the X-shaped plate was deflected with the maximum amplitude, a bending about its axis of symmetry could be seen (Fig. 11). This anticlastically bent part stiffened this plate region. It performed like a shell, and the fracture line was forced outwards toward the clamped boundaries. The flared ends and the slightly rounded clamping blocks reduced the stresses directly at the boundaries, so that no fracture could occur at those locations.

From all these effects, it was expected that it would not be simple to describe the behaviour mathematically exact if no empirical factors should be used.

2.3. Analysis and Design

In the elastic region, the load-displacement relation for the X-shaped device is linear up to the yield point of

$$d = \frac{6P \left(\frac{L}{2}\right)^3}{Ebt^3} \quad \text{from (5)} \quad (2.1)$$

(symbols see Fig. 8).

In the inelastic region, the proportionality between load and displacement no longer holds. However, before strain hardening starts, the yield plateau is fairly fat with an upper limit of an ultimate load of 1.5 times the yield load. This load was reached after approx. 0.1 to 2.5 times the yield displacement, depending on the thickness/length ratio. But this described only the behaviour of the energy absorber in an undamaged, fully operational state. In order to establish a relation between the maximum number of cycles to failure N and the maximum strain in the outer fibres of the device during each cycle a lower bound was found empirically (Fig. 7):

$$\epsilon_{\text{MAX.}} = \frac{0.22}{\sqrt{N}} \quad (2.2)$$

This formula is of highest importance for the designer and represents one of the major results of this thesis. The actual strain of the outer fibres of the device is a function of the maximum end-displacements d . Starting with the geometric relation of bending radius ρ and d :

$$\rho = \frac{4\left(\frac{d}{2}\right)^2 + L^2}{4d} \quad (2.3)$$

The curvature of one section is given by:

$$\phi = \frac{1}{\rho} = \frac{\varepsilon}{(t/2)} \quad (2.4)$$

and then the strain as

$$\varepsilon = \frac{t}{2\rho} = \frac{2dt}{d^2 + t^2} \quad (2.5)$$

This would be true for a double circular deflected shape and ideal boundary conditions. Both could only approximately be achieved in the experimental tests and do not apply for practical use. An empirical correction factor is suggested, which gives good correlation (see Table 3 and Fig. 12) with experimental measurements:

$$\varepsilon = \frac{2dt}{d^2 + t^2} \sqrt[3]{\frac{d}{3}} \quad (2.6)$$

It can be seen that for most earthquakes a design of an energy absorber with maximum strain of 2% is quite sufficient because we still cover 100 excitations to the maximum amplitude. For structures of extremely high importance, it is suggested that the maximum strain in the energy absorber to be reduced to 1.4 - 1.6% in order to achieve a higher factor of safety.

CHAPTER 3

YIELD RING

3.1. Description of Function

The second type of energy absorbing device consisted of two curved plate in pairs like rings with planes perpendicular to each other (Fig. 13). This enabled energy absorption in any horizontal and even vertical direction, which was the logical evolution of the one-directional device described above. The main goal was to design an element, which shows a stable behaviour, that is, after having experienced elastic and plastic deformation and being brought back to the initial position, the geometric shape of the device should not have changed. The anticipated bending moment distribution was approximately matched by the moment resistances of the deformed plates. This type of energy absorber was aimed at the application in base isolated structures, where bearing pads like roller bearings undergo lateral parallel displacements or rubber pads where even three-directional displacements had to be accommodated. The following requirements for the design, being the same as those for the one-directional device, were governing: the material should be steel with a high ductility, it should have an adequate fatigue life, temperature independance, and it should be possible not only to predict the yield behaviour but the life span, too.

3.2. Experimental Investigations and Results

The second focal point of my investigations was the curved plate

energy absorbers, in the following referred to yield rings. Their action was a combined bending-torsion action. The torsion was kept small by devising high length/thickness ratios.

Experimental tests for the case of fixed boundaries (see Fig. 13) have been conducted by [1] and lead to a simple analytical approach and result. My studies were mainly concerned about the case, when vertical and two-directional horizontal displacements would occur simultaneously. In this case, no fixed boundaries and no fixed curvature ρ were given. To simplify the interpretation of the experimental results, my tests were designed to be conducted without fixed boundaries, thus simulating the case for $d_{\text{vert}} = 0$. However, the deflected shape (see Fig. 14) and the location of fracture (see Fig. 15) seems not be favourable, if a maximum use of the material is desired. For practical applications, I would like to suggest a double tapered curved yield ring, which promises a much better long cycle behaviour, because yielding would occur over the full length of the ring. Due to the limited time available to conduct this thesis, the tests with this type of yield ring could not be finished, but it is strongly recommended to pursue this type in future investigations. The efficiency (absorbed energy per volume material) will be much greater, if not only two plastic hinges develop but the full length of the device is utilized.

The same test rig and measurement equipment like for the X-shaped energy absorber were used. The set-up is shown in Fig. 16 - Fig. 19. Only one quarter of a double yield ring was tested at a time. The ends of the half rings were displaced parallel (not on an arc like the X-shaped energy absorbers). Low cycle fatigue tests and strain

measurements were conducted. Fracture occurred at the locations of the plastic hinges (see Fig. 15) after a number of cycles, which can be predetermined (see Chapter 3.3).

For excitation in two directions (Fig. 20) the tests showed, that only very small reductions for the maximum number of cycles have to be taken into account. For the example of a bias of 3 in and 2.5 in cyclic displacement, the number of cycles to failure were reduced only about 6%. Although this agrees with the theoretically expected value, more tests will be required to establish a more exact design formula. For the being, it is suggested to use Eq. 2.2 even at 100% bias for the design. The results are still conservative enough.

3.3. Analysis and Design

The bending action of the yield rings resulted in the formation of plastic hinges at the boundaries (see Fig. 13). This location is fixed for any magnitude of stroke, that means the plastic hinge shifted from A to B. As it was shown in [1] that for high length/thickness ratios the axial force can be neglected, we were dealing with the simple situation of an ideal plastic hinge for which the amount of rotation was limited. So the maximum strain

$$\epsilon = \frac{t}{2R} \quad R = \rho \quad (3.1)$$

was independent from the stroke d . However, when the vertical stroke was allowed simultaneously, then the radius R was no longer constant and the rings developed plastic hinges at their clamped attachments (see Fig. 21).

In the case of omitted boundaries (Fig. 14) and inelastic deformation of the yield ring the following geometrical relations can be found: If the displacement d is larger than the yield displacement d_y , then the straight segment $AB = L$ of the plate can be approximated as a circular arc AB . This assumption is reasonable, because the cross section is uniform. For a certain displacement d at one end of the ring, the centre of the ring C will displace from location C to C' . The secant AC moves to AC' rotating about A with the angle α as the plastic hinge forms at A . So

$$\alpha = \alpha_1 - \alpha_2 \quad (3.2)$$

with

$$\alpha = \sin^{-1} \frac{(L+R)}{\sqrt{R^2 + (L+R)^2}} - \sin^{-1} \frac{(L+R) - \frac{d}{2}}{\sqrt{R^2 + (L+R - \frac{d}{2})^2}} \quad (3.3)$$

while point B moves to B' rotating about B

$$BB' = L\alpha = e \quad (3.4)$$

The radius of the arc AB' is found by

$$\rho = \frac{4e^2 + (2L)^2}{8e} = \frac{L(\alpha^2 + 1)}{2\alpha} \quad (3.5)$$

and the curvature of the shape is given by

$$\phi = \frac{1}{\rho} = \frac{\epsilon}{(t/2)} \quad (3.6)$$

with t = thickness of the yield ring.

Therefore, the strain is given by

$$\varepsilon = \frac{1}{\rho} \cdot \frac{t}{2} = \frac{\alpha t}{L(\alpha^2 + 1)} \quad (3.7)$$

If the error caused by assuming a circular shape for segment AB is considered, this has to be corrected by a factor found empirically as

$$\varepsilon = \frac{\alpha t}{L(\alpha^2 + 1)} \sqrt[3]{\frac{d}{15}} \quad (3.8)$$

This formula is not very convenient for practical design and a simplification in case of $L = R/2$ is proposed

$$\alpha = \sin^{-1} \frac{L+R}{\sqrt{R^2 + (L+R)^2}} - \sin^{-1} \frac{(L+R) - d/2}{\sqrt{R^2 + (L+R - d/2)^2}} \quad (3.9)$$

$$\alpha = \sin^{-1} \frac{1.5 R}{\sqrt{R^2 + 1.5 R^2}} - \sin^{-1} \frac{1.5 R - d/2}{\sqrt{R^2 + (1.5 R - d/2)^2}} \quad (3.10)$$

$$\text{with} \quad m = d/R \quad (3.11)$$

and finally

$$\alpha = 0.983 - \sin^{-1} \frac{1.5 - (m/2)}{\sqrt{1 + [1.5 - (m/2)]^2}} \quad (3.12)$$

or

$$\alpha = f(m) \quad (3.13)$$

This theoretical relation is in good correlation with the measured values (see Fig. 22 and Table 4).

In summary, knowing the displacement d the value of α can be obtained by eq. 3.12 and the strain ϵ by eq. 3.8.

The same formula Eq. (2.2) for establishing the maximum number of cycles to failure is valid for the yield rings and shows a very good correlation to the experimental results for this type of solid state steel energy absorber (Fig. 7). It represents a lower bound, thus giving conservative design values.

CHAPTER 4

IMPLEMENTATION OF YIELD RINGS4.1 Description of Experimental Set-Up

In the preceding chapters the characteristics and analysis of the x-shaped energy absorber and the yield rings were described, separated from the practical application. While the application in a structure was investigated in [4] for the x-shaped energy absorber, this chapter now is going to set the yield rings in context with a practical use. Both devices can be used in a multitude of applications. The implementation as a wind restraint and displacement limitation in a building or structure subjected to seismic loads is only one practical example.

The purpose of the test described in the following was to serve as a basis for a correlation study with an analytical method for the design of the yield rings depending on the magnitudes of the expected earthquakes and the size of the buildings.

A model of a steel building with a moment resisting frame was used, which was the main subject of other investigations and is described in detail in [7]. The overall dimensions of the frame were 10 ft x 4.6 ft in plan and 12.8 ft in height. Three of the four floors were loaded with concrete blocks, resulting in a total mass of the structure of 16 kips. A base-isolating system was implemented in this building, which the main component consisted of steel roller bearings (see Figs. 23 and 24). These elements had a static friction coefficient of $\mu_s = .2/16 = .012$ and a kinetic friction coefficient of $\mu_k = .1/16 = .006$. Two return springs were installed, each with a

stiffness of 90 lbs/in.

This structure was placed on the earthquake simulator facility of the Department of Civil Engineering, University of British Columbia. The shaking table has the floor dimensions of 10 ft x 10 ft and a maximum capacity of 30.5 kips for test models. Up to this mass a maximum acceleration of 2.5 g with peak-to-peak displacements of 2.5 in can be achieved. An MTS hydraulic system drives the table which can be controlled either by a function generator for regular waveforms or by a minicomputer (PDP 11/04) for time histories of real or artificial earthquake. Currently approximately 150 different earthquake records are readily accessible in digital form.

During a sequence of tests five different yield ring sets were tested. The yield rings were placed in parallel with the base isolation system (see Figs. 25 and 26). The dimensions and characteristic values are shown in Tables 5 and 6.

4.2 Analytical Modelling

The model steel frame, which I used, responded to ground excitation primarily like a single degree of freedom system, due to its relatively rigid frame and base-isolating system with soft yield rings. If the damping provided by the yield rings is described in a form of equivalent viscous damping C_{eq} , the system can be modelled like in Fig. 27. For very small stiffness K and damping this representation of the displacement dependent damping (see hysteresis loop in Fig. 28) should be allowed. For this single degree of freedom system the description of its response due to a ground motion is straight forward. The differential equation of the motion is given as

$$M \ddot{x}_a + C_{eq} \dot{x}_a + K x_a = C_{eq} \dot{x}_g + K x_g \quad (4.1)$$

and then the equivalent damping ratio ξ_{eq} follows as

$$\xi_{eq} = \frac{C_{eq}}{2 M \omega_n} \quad (4.2)$$

with the natural frequency

$$\omega_n = \sqrt{\frac{K}{M}} \quad (4.3)$$

Eq. 4.1 can be reformulated as

$$\ddot{x}_a + 2 \xi_{eq} \omega_n \dot{x}_a + \omega_n^2 x_a = 2 \xi_{eq} \omega_n \dot{x}_g + \omega_n^2 x_g \quad (4.4)$$

To determine the transfer function $H(\omega)$ for this system let

$$\ddot{x}_g = e^{i\omega t} \quad (4.5)$$

Then $\ddot{x}_a = H(\omega) e^{i\omega t}$ and (4.6)

$$H(\omega) = \frac{\ddot{x}_a}{\ddot{x}_g} = \frac{\sqrt{1 + \left(2 \xi_{eq} \frac{\omega}{\omega_n}\right)^2}}{\sqrt{\left[1 - \left(\frac{\omega}{\omega_n}\right)^2\right]^2 + \left(2 \xi_{eq} \frac{\omega}{\omega_n}\right)^2}} \quad (4.7)$$

Because this transfer function mainly represents the performance of the isolating system and the yield rings, it is called in the following "acceleration attenuation ratio" AR. It is possible to solve Eq. 4.7 for the equivalent damping

$$\xi_{eq} = \frac{1}{2\left(\frac{\omega}{\omega_n}\right)} \sqrt{\frac{1 - AR^2 \left[1 - \left(\frac{\omega}{\omega_n}\right)\right]^2}{AR^2 - 1}} \quad (4.8)$$

The acceleration attenuation ratio $AR = H(\omega)$ and the equivalent damping can be used to develop a design procedure for the yield rings.

Firstly, I have to find the relation between the relative displacement du between ground and structure and the equivalent damping ξ_{eq} of the yield rings.

$$d_u = x_a - x_g \quad (4.9)$$

Now the basic differential equation of motion can be written as

$$M \ddot{d}_u + C_{eq} \dot{d}_u + K d_u = -M \ddot{x}_g \quad (4.10)$$

Dividing this by M

$$\ddot{d}_u + 2\xi_{eq}\omega_n \dot{d}_u + \omega_n^2 d_u = -\ddot{x}_g \quad (4.11)$$

The transfer function is found by letting

$$\ddot{x}_g = e^{i\omega t} \quad (4.12)$$

and

$$d_u = G(\omega) e^{i\omega t} \quad (4.13)$$

Substituting this into Eq. 4.11

$$G(\omega) = \frac{du}{\ddot{x}_g} = \frac{1}{\omega_n^2 \sqrt{[1 - (\frac{\omega}{\omega_n})^2]^2 + (2 \zeta_{eq} \frac{\omega}{\omega_n})^2}} \quad (4.14)$$

The equivalent damping was given by Eq. 4.8. Solving for the maximum absolute value of displacement $|du|$:

$$|du| = \frac{|\ddot{x}_g|}{\omega^2} \sqrt{\frac{(1 - AR^2)(\frac{\omega}{\omega_n})^2}{[(\frac{\omega}{\omega_n})^2 - 2]}} \quad (4.15)$$

This can be expressed as

$$du = |x_g| \cdot \gamma \quad (4.16)$$

where the maximum absolute displacement of the exciting ground is

$$|x_g| = \frac{|\ddot{x}_g|}{\omega^2} \quad (4.17)$$

and the displacement factor is

$$\gamma = \sqrt{\frac{(1 - AR^2)(\frac{\omega}{\omega_n})^2}{[(\frac{\omega}{\omega_n})^2 - 2]}} \quad (4.18)$$

which is plotted in Fig. 29 for different attenuation ratios. It can be seen, that for

$$\text{if } (\frac{\omega}{\omega_n}) = \sqrt{2} \quad \text{then} \quad \gamma \rightarrow \infty \quad (4.19)$$

This can be looked upon as the limit state for our design. It shows that for a more effective acceleration attenuation a greater amount of energy has to be absorbed by the yield rings, however this is nonlinear related. As it will be seen later, this theoretical value could be verified by experiments with a good accuracy.

Several methods for deriving the equivalent damping from a load-displacement hysteresis loop have been tried. The damping is directly related to the enclosed area of the hysteresis loop. This area is approximately

$$A_D = 4 P_Y (d_u - d_y) = 4 P_Y d_u \left(1 - \frac{1}{\mu}\right) \quad (4.20)$$

with

$$\mu = \frac{d_u}{d_y} \quad (4.21)$$

which will be called ductility factor of the yield ring. The equivalent viscous damping amounts to

$$C_{eq} = \frac{A_D}{\pi d_u^2 \omega} = \frac{4}{\pi} \left(1 - \frac{1}{\mu}\right) \frac{P_Y}{d_u \omega} \quad (4.22)$$

The equivalent damping ratio can be written as

$$\xi_{eq} = \frac{4}{\pi} \left(1 - \frac{1}{\mu}\right) \frac{P_Y}{d_u \left(\frac{\omega}{\omega_n}\right)} \cdot \frac{1}{2 M \omega_n^2} \quad (4.23)$$

note:

$$M\omega^2 = K \quad (4.24)$$

$$\frac{P_y}{K} = d_y \quad (4.25)$$

With this the equivalent damping ratio can be simplified

$$\xi_{eq} = \beta \frac{1}{\left(\frac{\omega}{\omega_n}\right)} \quad (4.26)$$

with

$$\beta = \frac{2\left(1 - \frac{1}{\mu}\right)}{\pi \mu} \quad (4.27)$$

The expression β will be called absorber damping factor, which depends on the ductility factor μ of the yield ring and represents the equivalent damping ratio of the system. When this is displayed as a function in Fig. 30, it can be seen, that the damping factor has its maximum value for $\mu = 2$, which is the critical absorber damping factor. For higher values of μ the damping factor decreases. It seems to be effective in design to aim at this value.

If Eq. 4.26 is combined with Eq. 4.7 the acceleration attenuation factor AR is

$$AR = \frac{\ddot{x}_a}{\ddot{x}_g} = \sqrt{\frac{1 + 4\beta^2}{4\beta^2 + \left[1 - \left(\frac{\omega}{\omega_n}\right)^2\right]^2}} \quad (4.28)$$

4.3 Test-Results and Proposal for Yield Ring Design

The test series included regular sine-wave excitations and

earthquake time-histories (see Tables 7 and 8).

The summary of the sine-wave excitation is shown in Table 9. The table shows the correlation values for relative displacements, and it has to be noted, that the theoretical value are quite conservative. In Table 10 and Fig. 31 the measured values are compared with those theoretically expected. The ratio of attenuation ratios shows, that for different yield ring systems and excitation frequencies a relatively good correlation could be achieved. Theoretical values are slightly higher. This error was traced to come from the choice of the representative acceleration of the structure. If the average value for the whole structure would have been taken, instead of the first storey value, the correlation would have been even better.

In the case of earthquake excitation the predominant frequency of the earthquake spectrum should be taken as the exciting frequency. In my test series this resulted in a slightly too smaller attenuation ratio for the theoretical value than the measured value, which can be explained by the fact, that the exact exciting frequency ω is lower than the predominant frequency ω_p . To correct for this error the correction factor $\sqrt{\frac{\omega_p}{\omega_n}}$ should be used, which yields better results for AR

$$AR = \frac{\ddot{x}_a}{\ddot{x}_g} = \sqrt{\frac{1 + 4\beta^2}{4\beta^2 + \left[1 - \left(\frac{\omega_p}{\omega_n}\right)^2\right]^2}} \cdot \sqrt{\frac{\omega_p}{\omega_n}} \quad (4.29)$$

with ω_n - natural frequency of the system (RADS./S.)

ω_p - predominant frequency of the earthquake excitation (RADS./S.)

β - absorber damping factor from above.

The comparison is listed in Table 11 and plotted in Fig. 32 for the following earthquake excitations: El Centro, San Fernando, Parkfield (each with different damping arrangements). The modified Eq. 4.28 yields conservative values for AR for the design. Theoretically for most modern flexible structures with low natural frequencies these earthquakes would be rather dangerous, but my experimental results indicate, that particularly in the low frequency area a higher safety reserve is actually existing.

In the following a summary of the design procedure is described. For a given characteristical acceleration a_g for a specific building site and the desired return period (e.g. 50 or 100 years) and the desired (or maximum allowable) acceleration a_d of the structure the acceleration attenuation ratio is calculated, representing the basic design parameter. Now an energy absorbing system has to be designed, thus determining the basic properties of the energy absorber with m , c , and K . The damping factor β can be computed and the design attenuation ratio AR. An acceptable design is achieved when $AR \leq [AR]$ and the number of cycles to failure N is large enough (100-300). A step-by-step procedure would have the following detailed sequence:

- 1) Determine the maximum ground acceleration a_g and the predominant frequency f_g of the expected design earthquake.

The maximum ground acceleration a_g depends on the expected earthquake magnitude M and the expected distance R from the epicentre of the building site. These values can be obtained from the design codes or approximately by computation ([13] and [14])

$$\ddot{x}_g = \frac{1080 e^{0.5M}}{(R+25)^{1.32}} \quad (4.30)$$

or

$$\ddot{x}_g = \frac{5600 e^{0.8M}}{(R+40)^2} \quad (4.31)$$

An alternative method is presented in [16] and [17], in case the area is divided in zones, for which a Mercalli Intensity Scale is determined (see Table 12).

The predominant frequency ω_p depends on local soil conditions. From the Table 13 values for the predominant period T_p can be taken, which related to the frequency by

$$\omega_p = \frac{2\pi}{T_p} \quad (4.32)$$

or in case the depth of the soil layer H and average velocity of a shear wave is known

$$T_p = \frac{4H}{v_s} \quad (\text{from [12]}) \quad (4.33)$$

2) Determine the maximum allowable acceleration response of the structure.

In the case of a base isolated building, like described in this thesis, the building can be represented by a single degree of freedom system. The limiting acceleration can be taken as the maximum value from the National Building Codes for Structures not requiring special design considerations for earthquake loads. Typically this corresponds with the modified Mercalli Intensity Scale V with a maximum design acceleration of 0.021 g (see Table 31). For this "general case" and

for buildings of very high importance a safety factor ranging from 1.5 to 3.0 should be considered, if not otherwise specified.

3) Design the isolating and energy absorbing system.

Isolators:

Any isolating system (rubber pads, sliding pads, roller bearings, etc.) can be used. Current research [7] indicates, that the roller bearings have a slight edge above the other systems what reliability, stability, availability, and cost is concerned.

Energy Absorbers:

Start the design with a trial value for the thickness t , width b , radius R and length L (recommendations see previous chapters) of the yield ring. A good value for the radius is $R > 10 t$ (from [18]).

Now compute the yield force

$$P_y = \frac{\epsilon_y E}{6K} \cdot b t^2 \quad (4.34)$$

The yield displacement is given by

$$d_y = \frac{P_y}{K} \quad (4.35)$$

and the stiffness by

$$K = \sqrt{\frac{E b t^3}{48 R^2 (L - 0.52 R)}} \quad (4.36)$$

The Young's modulus should be taken as 28000 ksi and the yield strain as .002 for mild steel. Now the natural frequency ω_n can be calculated, where M is the mass of the structure. A recommended value

for the yielding force is 5% of the weight of the structure, if not specified by the value for the wind restraint.

- 4) Determine the damping factor β of the yield rings.

After the maximum displacement du of the yield ring has been computed by using Eq. 4.15 or Eq. 4.16 or taken from Fig. 4.7, check the geometry for the maximum extended position of the yield ring. It should be just about to loose its curved shape, thus starting to act in tension rather than bending to act as a soft stop. With the ductility factor $\mu = \frac{du}{dy}$ the damping factor is found from Eq. 4.27 or taken from Fig. 4.8.

- 5) Check the acceleration attenuation ratio.

The value of the acceleration attenuation ratio AR associated with the desired design can now be computed by Eq. 4.29 and the condition $AR \leq [AR]$. If this is not satisfied, choose new trial values for yield ring.

- 6) Check the earthquake resistant performance of the yield rings.

The maximum number of cycles to failure should generally be not smaller than 100 if not exactly determined by site conditions and life span of the building. Then Eqs. 2.2 and 3.8 can be used. The described procedure can be used without the availability of computer analysis. However, the development of an interactive, computer aided design approach seems to be desirable and is hopefully subject of continuing research.

CHAPTER 5

CONCLUSIONS

A comprehensive study of all available data of our own test results and from others leads to the following general conclusions:

Solid state steel energy absorbing devices represent an efficient, inexpensive, reliable, and maintenance free means for providing damping in flexible or base-isolated buildings.

Design formula are now available, which describe the yield load, the strain level, and the life span simply and accurately enough to be used for engineering purposes.

Both devices under investigation act in the same sequence: elastically up to the yield point, plastically with small amounts of elasticity (slightly sloped yield plateau), and finally due to strain hardening and geometrical deformation as a soft stop for excessive deflections.

The one-directional X-shaped energy absorber, which has no hinged connection rods like previous designs, is insensitive to limited torsional action.

The multi-directional double yield rings enable energy absorption in any horizontal and vertical direction.

Earthquake excitation forces can be greatly reduced in buildings or structures when flexible systems with energy absorbers or base-isolated system with wind restraint and displacement limitations are used (Figs. 33 and 34).

The energy absorbing devices can be designed for any type of

earthquake and rate of energy absorption.

Possible damage is restricted to special replaceable devices. The main structure remains elastic during all types of excitations and requires only linear elastic analysis.

The energy absorbing devices can be retrofitted into existing buildings and structures, to upgrade the earthquake resistance. Implementation into new structures results very likely in considerable savings and higher safety. A case study would be an interesting topic for a future research project.

CHAPTER 6

REFERENCES

- [1] Kelly, J.M., Skinner, R.I., Heine, A.J.: Mechanisms of Energy Absorption in Special Devices for Use in Earthquake Resistant Structures, in Bulletin of the New Zealand Society for Earthquake Engineering, Vol. 5, No. 3, 63-88, Sept. 1972.
- [2] Kelly, J.M., and Skinner, J.S.: The Design of Steel Energy Absorbing Restrainers and Their Incorporation into Nuclear Power Plants for Enhanced Safety, Vol. 4, A Review of Current Uses of Energy-Absorbing Devices, Report No. UCB/EERC-79/10, Earthquake Engineering Research Center, University of California, Berkeley, Feb. 1979.
- [3] Stierner, S.F., and Godden, W.G.: The Design of Steel Energy Absorbing Restrainers and Their Incorporation into Nuclear Power Plants for Enhanced Safety, Shaking Table Tests of Piping Systems with Energy-Absorbing Restrainers, UCB/EERC-80/33, Earthquake Engineering Research Center, University of California, Berkeley, Sept. 1980.
- [4] Stierner, S.F., Godden, W.G., and Kelly, J.M.: Experimental Behaviour of a Spatial Piping System With Steel Energy Absorbers Subjected to a Simulated Differential Seismic Input, UCB/EERC-81/09, Earthquake Engineering Research Center, University of California, Berkeley, July 1981.
- [5] Schneider, S., Lee, H.M., and Godden, W.G.: Behaviour of a Piping System Subjected to Seismic and Thermal Loading, in Proceedings of

- the Fourth Canadian Conference of Earthquake Engineering, p. 140-150, Vancouver, Canada, June 1983.
- [6] Zackay, V.F., Kelly, J.M., Penzien, J., Powell, G., Wilson, E.L., Bush, S.H., Finnle, I., and Stiemeier, S.F.: The Design of Steel Energy Absorbing Restrainers and Their Incorporation into Nuclear Power Plants for Enhanced Safety, Prepared for the Department of Energy under Contract DE-AS03-76SF00035 PA DE-AT03-ER70296, College of Engineering, University of California, Berkeley, California Progress Report, March 1980, Section 2, 2-5 - 2-12.
 - [7] Barwig, B.B., and Stiemeier, S.F.: Base Isolation Design for Earthquake Resistant Steel Buildings, Proceedings of the Fourth Canadian Conference of Earthquake Engineering, p. 382-391, Vancouver, Canada, June 1983.
 - [8] Kelly, J.M., Skinner, M.S., and Beucke, K.E.: Experimental Testing of an Energy-Absorbing Base Isolation System, Report No. UCB/EERC-80/35, Earthquake Engineering Research Center, University of California, Berkeley, Feb. 1979.
 - [9] Tyler, R.G.: A Tenacious Base Isolation System Using Round Steel Bars, Bulletin of the New Zealand National Society for Earthquake Engineering, Vol. 11, No. 4, Dec. 1978.
 - [10] Tyler, R.G.: Tapered Steel Energy Dissipators for Earthquake Resistant Structures, Bulletin of the New Zealand National Society for Earthquake Engineering, Vol. 11, No. 4, Dec. 1978.
 - [11] Dowrick, D.J.: Earthquake Resistant Design, John Wiley & Sons Ltd., 1977, 374 p.
 - [12] Bolotin, V.V.: Statistical Theory of a Seismic Design of Structures, Proc. Second World Conference on Earthquake

Engineering, Tokyo, 2, 1365-1374, 1960.

- [13] Amin, M., and Ang, A.H.S.: A Nonstationary Stochastic Model for Strong-Motion Earthquakes, Structural Research Series No. 306, University of Illinois, Department of Civil Engineering, April 1966.
- [14] Seed, H.B., Ugas, C., and Lysmer, J.: Site Dependent Spectra for Earthquake Resistant Design, Report No. UCB/EERC-74/12, Earthquake Engineering Research Center, University of California, Berkeley, Nov. 1974.
- [15] Ambraseys, N.N.: Dynamics and Response of Foundation Materials in Epicentral Regions of Strong Earthquakes, Proc. 5th World Conference on Earthquake Engineering, Rome, 1, CXXVI-CXLVIII, 1973.
- [16] Okamoto, S.: Introduction to Earthquake Engineering, University of Tokyo Press, 1973.
- [17] Singer, F.L. and Pytel, A.: Strength of Materials, Third Edition, 1980.
- [18] Barwig, B.B.: Experimental Investigation of the Base Storey Design of Base Isolated Steel Buildings, Department of Civil Engineering, University of British Columbia, Canada, Nov. 1983.

	LENGTH	WIDTH AT ROOT	THICKNESS	STROKE	THERMAL BIAS	CYCLES/ T.B.
TEST	L	W	T	S	TB	CTB
Q1	5	L/2	1/4	L/4	0	0
Q2	5	L/2	1/4	L/4	0	0
Q3	5	L/2	1/4	L/4	0	0
Q4	5	L/2	1/4	L/4	0	0
Q5	5	L/2	1/4	L/4	0	0
T1	5	L/2	1/8	L/4	0	0
T2	5	L/2	3/16	L/4	0	0
T3	5	L/2	1/4	L/4	0	0
T4	5	L/2	5/16	L/4	0	0
S1	5	L/2	1/4	L/10	0	0
S2	5	L/2	1/4	L/5	0	0
S3	5	L/2	1/4	3L/10	0	0
S4	5	L/2	1/4	2L/5	0	0
S5	5	L/2	5/16	L/10	0	0
S6	5	L/2	5/16	L/5	0	0
S7	5	L/2	5/16	3L/10	0	0
S8	5	L/2	5/16	2L/5	0	0
L1	2	L/2	1/4	L/4	0	0
L2	3	L/2	1/4	L/4	0	0
L3	4	L/2	1/4	L/4	0	0
L4	5	L/2	1/4	L/4	0	0
L5	6	L/2	1/4	L/4	0	0
L6	7	L/2.6	1/4	L/4	0	0
L7	8	L/2.6	1/4	L/4	0	0
TB1	5	L/2	1/4	L/4	L/10	0
TB2	5	L/2	1/4	L/4	L/5	0
TB3	5	L/2	1/4	L/4	3L/10	0
TB4	5	L/2	1/4	L/4	2L/5	0
CTB	5	L/2	1/4	L/5	0	50
					+L/5	50
					0	50
					-L/5	50
R1	5	2L/5	1/4	L/4	0	0
R2	5	L/2	1/4	L/4	0	0
R3	5	2L/5	1/4	L/4	0	0

Table 1: Dimensions of X-Shaped Energy Absorber

SPECIMEN	du (in)	t (in)	L (in)	ϵ_{\max} (from 2-6)	N (from test)
Q1~Q2	1.25	0.25	5	0.0176	177,178,230, 253,292
T1	1.25	0.125	5	0.0088	126
T2	1.25	0.1875	5	0.0132	364
T3	1.25	0.25	5	0.0351	301
T4	1.25	0.3125	5	0.0468	182
S1	0.5	0.25	5	0.011	1710
S2	1.0	0.25	5	0.0266	466
S3	1.5	0.25	5	0.0436	179
S4	2.0	0.25	5	0.0602	114
S5	0.5	0.3125	5	0.0136	1173
S6	1.0	0.3125	5	0.0333	298
S7	1.5	0.3125	5	0.0546	144
S8	2.0	0.3125	5	0.0751	72
L1	0.5	0.25	2	0.0638	42
L2	0.75	0.25	3	0.0491	138
L3	1.0	0.25	4	0.0402	124
L4	1.25	0.25	5	0.0351	276
L5	1.50	0.25	6	0.0311	229
L6	1.75	0.25	7	0.0281	404
L7	2.0	0.25	8	0.0257	431
R1~R3	1.25	0.25	5	0.0351	134,263,173
TB1	1.75	0.25	5	0.0521	277
TB2	2.25	0.25	5	0.0672	229
TB3	2.75	0.25	5	0.0816	168
TB4	3.25	0.25	5	0.0939	142
CA1~CA5	0.5	0.125	2	0.0407	147,189,161, 185

* ϵ_{\max} of Q1~Q2 is from measurement. Others from calculation using formula (2-6).

Table 2: Low Cycle Fatigue Test Results

DISPLACEMENT d*** (in)	THEORETIC VALUES ϵ FROM (2-6) (10^{-6})	MEASURING VALUE [ϵ] POINT 34 IN FIG. 6 (10^{-6})	$\epsilon/[\epsilon]$
0.125	866	956	0.91
0.250	2178	2130	1.02
0.375	3729	3775	0.99
0.500	5448	5463	0.99
0.625	7298	7322	0.99
0.75	9242	9416	0.98

** This plate is shown in Fig. 6. $L=5"$, $t=1/4"$.

*** d is shown in Fig. 8.

Table 3: Theoretical and Experimental Values of Strain for
X-Shaped Energy Absorber

DISPLACEMENT d*** (in)	ANGLE VALUE α FROM (3.12)	THEO. VALUE ϵ FROM (3-8)	MEASURING VALUE [ϵ] POINT 1 IN FIG. 19	$\epsilon/[\epsilon]$
1.0	0.0480	0.0021	0.002114	0.99
1.25	0.0518	0.0028	0.002878	0.47
1.65	0.0700	0.0042	0.003774	1.12
2.0	0.0867	0.0055	0.005808	0.95
2.5	0.1119	0.0076	0.007350	1.03

** This plate is shown in Fig. 19. $L=2"$, $R=4"$, $t=1/4"$

*** d is shown in Fig. 14.

Table 4: Theoretical and Experimental Values of Strain for
Yield Ring

					pseudo static test	
NO. OF PLATES	R (in)	L (in)	t (in)	b (in)	k (kips/in)	P _y (kips)
E1	3	1.5	1/8	1.25	0.067	0.0625
E2	3	1.5	3/16	1.25	0.133	0.125
E3	3	1.5	1/4	1.25	0.200	0.25

Table 5: Dimension of Yield Rings Used in Low Cycle Fatigue Tests

COMBINE PLATES OF SYSTEM	STIFFNESS OF SYSTEM K (kips/in)	YIELDING FORCE OF SYSTEM P _y (kips)	NATURAL FREQUENCY OF SYSTEM** f (Hz)
8E1	0.72	0.62	0.61
4E2	0.71	0.60	0.76
6E2	0.98	0.85	0.83
2E3	0.78	0.80	0.90
4E3	0.98	1.10	1.16

* K, P_y, ω_n consider the stiffness of springs and friction of rollers besides curved plates.

** Natural frequencies have been checked with a "free vibration test"

Table 6: Stiffness, Yield Force and Natural Frequencies for Different Yield Ring Combinations

FREQUENCY ω (Hz)	MAX. ACCELERATION OF TABLE \ddot{X}_g (g)	MAX. DISPLACEMENT OF TABLE X_g (in)
1.0	0.178	1.475
2.0	0.656	1.463
3.0	1.96	1.440
4.0	2.089	0.948

Table 7: Peak Values for Accelerations and Displacement of
Sinusoidal Table Excitation Used for Tests

NAME OF E/Q RECORDS	PREDOMINANT FREQUENCY RANGE** ω (Hz)	MAX. ACCELERATION* OF TABLE \ddot{X}_g (g)	MAX. DISPLACEMENT OF TABLE X_g (in)
EL CENTRO	1.2 ~ 2.2 (1.5)	0.349	1.749
SAN FERNANDO	4.0 ~ 5.7 (4.0)	0.793	1.076
PARKFIELD	0.6 ~ 2.3 (1.5)	0.233	1.704

** From the Fourier Spectra of acceleration record.

* Only use the first 10 seconds of E/Q which included the peak value of acceleration.

Table 8: Peak Values for Accelerations and Displacements of
Earthquake Table Excitation Used for Tests

Energy Absorber System	Frequency of Sine-Wave Excitation (Hz)	$\left(\frac{\omega}{\omega_n}\right)$	$\frac{\ddot{x}_a}{\ddot{x}_g}$ (from test)	r	du (in)		$\frac{du}{[du]}$
					theor, du $= \frac{\ddot{x}_g}{\omega} \cdot \gamma$	measuring[du]	
8E1	0.6					2.106	
	3.0	1.33	0.45			1.399	1.19
	2.0	2.64	0.08	1.18	1.89	1.581	1.48
	0.9	3.95	0.03	1.07	2.28	1.538	
4E2	1.0	1.21	0.42			1.871	
	2.0	2.64	0.09	1.18	1.88	1.526	1.23
	3.0	3.95	0.03	1.07	2.28	1.531	1.49
6E2	1.0	1.21	0.56			1.946	
	2.0	2.41	0.13	1.23	1.97	1.604	1.23
	3.0	3.62	0.05	1.09	2.31	1.502	1.54
2E3	1.0	1.11	0.52			1.901	
	2.0	2.22	0.12	1.29	2.07	1.579	1.31
	3.0	3.34	0.04	1.10	2.34	1.492	1.57
	4.0	4.45				1.305	
4E3	1.0	0.86	0.87			2.114	
	2.0	1.73	0.20	1.70	2.72	1.668	1.63
	3.0	2.59	0.07	1.19	2.53	1.515	1.67
	4.0	3.45	0.05	1.10	0.94	0.957	0.98

Table 9: Displacement Ratios for Different Frequencies of Sinusoidal Excitation and Different Yield Rings

Energy Absorber System	Frequency			Absorber Damping Factor β				Theoretic. $AR = \frac{\ddot{x}_a}{\ddot{x}_y}$	Measured [AR]			Ratio AR/[AR]
	Table ω (Hz)	System ω_n^* (Hz)	$(\frac{\omega}{\omega_n})$	du (measured) (in)	dy (measured) (in)	$\mu = \frac{du}{dy}$	$\beta = \frac{2}{\pi} \frac{(u-1)}{\mu^2}$		$[\ddot{x}_g]$ (g)	$[\ddot{x}_a]**$ (g)	$[AR] = \frac{[\ddot{x}_a]}{[\ddot{x}_g]}$	
8E1	0.6	0.61	0.98	2.106	1.0	2.11	0.159	3.27	0.051	0.068	1.33	2.46
	0.9	0.61	1.48	1.399	1.0	1.40	0.150	0.85	0.108	0.049	0.45	1.89
	2.0	0.61	3.28	1.581	1.0	1.58	0.148	0.11	0.656	0.054	0.08	1.38
	3.0	0.61	4.92	1.538	1.0	1.54	0.145	0.04	1.96	0.054	0.03	1.33
4E2	1.0	0.76	1.32	1.871	0.75	2.49	0.153	1.30	0.178	0.074	0.42	3.10
	2.0	0.76	2.63	1.526	0.75	2.04	0.159	0.18	0.656	0.061	0.09	2.0
	3.0	0.76	3.95	1.531	0.75	2.04	0.159	0.07	1.96	0.066	0.03	2.33
6E2	1.0	0.83	1.20	1.946	0.75	2.60	0.151	1.96	0.178	0.100	0.56	3.50
	2.0	0.83	2.41	1.604	0.75	2.13	0.159	0.22	0.656	0.082	0.13	1.69
	3.0	0.83	3.61	1.502	0.75	2.00	0.159	0.09	1.96	0.090	0.05	1.80
2E3	1.0	0.90	1.11	1.901	0.6	3.17	0.137	2.89	0.178	0.092	0.52	5.56
	2.0	0.90	2.22	1.579	0.6	2.63	0.150	0.26	0.656	0.076	0.12	2.17
	3.0	0.90	3.33	1.492	0.6	2.48	0.153	0.10	1.96	0.079	0.04	2.50
	4.0	0.90	4.44	1.305	0.6	2.17	0.158	0.06	—	0.085		
4E3	1.0	1.16	0.86	2.114	0.6	3.52	0.129	2.82	0.178	0.154	0.87	3.24
	2.0	1.16	1.72	1.668	0.6	2.78	0.147	0.53	0.656	0.131	0.20	2.65
	3.0	1.16	2.58	2.515	0.6	2.53	0.152	0.18	1.96	0.135	0.07	2.57
	4.0	1.16	3.44	3.957	0.6	1.60	0.149	0.10	1.39	0.113	0.08	1.25

* Natural frequencies have been checked with a "free vibration test".

** $[\ddot{x}_a]$ is a measured value from accelerometer on first floor (A_1).

Table 10: Acceleration Response Attenuation Ratios for
Different Sinusoidal Excitations

Energy Absorber System	Earthquake	Frequency		Absorber Damping Factor β				Theoretic. $AR = \frac{\ddot{x}_a}{\ddot{x}_y}$	Measured [AR]			Ratio AR/[AR]
		Predominant Frequency of E/Q ω_p	System ω_n	du (in)	dy (in)	$\mu = \frac{du}{dy}$	β		$[\ddot{x}_g]$ (g)	$[\ddot{x}_a]**$ (g)	$[AR] = \frac{[\ddot{x}_a]}{[\ddot{x}_g]}$	
8E1	El Centro	1.5	0.61	2.46	2.84	1.0	2.84	0.323	0.349	0.091	0.26	1.24
	San Fernando	4.0	0.61	6.56	1.592	1.0	1.592	0.064	0.793	0.054	0.068	0.94
	Parkfield	1.3	0.61	2.13	2.34	1.0	2.34	0.431	0.233	0.091	0.391	1.10
4E2	El Centro	1.5	0.76	1.97	2.49	0.75	3.134	0.502	0.349	0.114	0.327	1.54
	San Fernando	4.0	0.76	5.26	1.504	0.75	2.159	0.090	0.793	0.059	0.074	1.22
	Parkfield	1.3	0.76	1.71	1.979	0.75	2.150	0.701	0.233	0.114	0.489	1.43
6E2	El Centro	1.5	0.83	1.81	1.774	0.75	2.155	0.613	0.349	0.101	0.289	2.12
	San Fernando	4.0	0.83	4.82	1.491	0.75	1.159	0.104	0.793	0.077	0.097	1.07
	Parkfield	1.3	0.83	1.57	2.083	0.75	2.147	0.874	0.233	0.161	0.691	1.27
2E3	El Centro	1.5	0.90	1.67	1.954	0.60	3.135	0.740	0.349	0.106	0.304	2.43
	San Fernando	4.0	0.90	4.44	1.547	0.60	2.151	0.118	0.793	0.070	0.088	1.34
	Parkfield	1.3	0.90	1.44	2.20	0.60	3.126	0.122	0.233	0.189	0.811	1.38
4E3	El Centro	1.5	1.16	1.29	1.939	0.60	3.136	0.640	0.349	0.155	0.444	3.69
	San Fernando	4.0	1.16	3.45	1.292	0.60	2.158	0.179	0.793	0.131	0.165	1.09
	Parkfield	1.3	1.16	1.12	1.607	0.60	2.149	0.818	0.233	0.139	0.597	4.72

Table 11: Acceleration Response Attenuation Ratios for
Different Earthquake Excitations

MM SCALE	\ddot{x}_g (%g)
V	1 ~ 2.1
VI	2.1 ~ 4.4
VII	4.4 ~ 9.4
VIII	9.4 ~ 20.2
IX	20.2 ~ 43.2
X	> 43.2

Table 12: Modified Mercally Intensity Scale

SOIL CONDITION	T_p (s)
Rock	0.1 ~ 0.15
Stiff soil	= 0.2
Deep cohesionless soils	= 0.3
Soft to medium clay and sand	= 0.7

Table 13: Predominant Frequencies for Different Soil Conditions

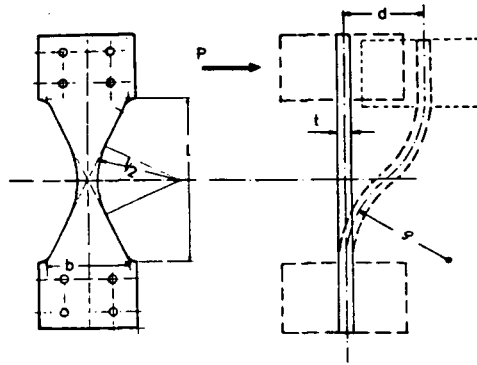


Fig. 1: X-Shaped Energy Absorber

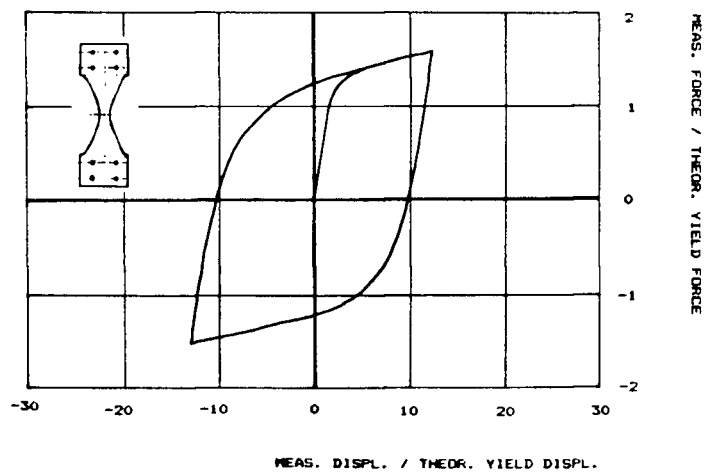


Fig. 2: Load-Displacement Hysteresis Loops for X-Shaped Energy Absorber and Yield Ring

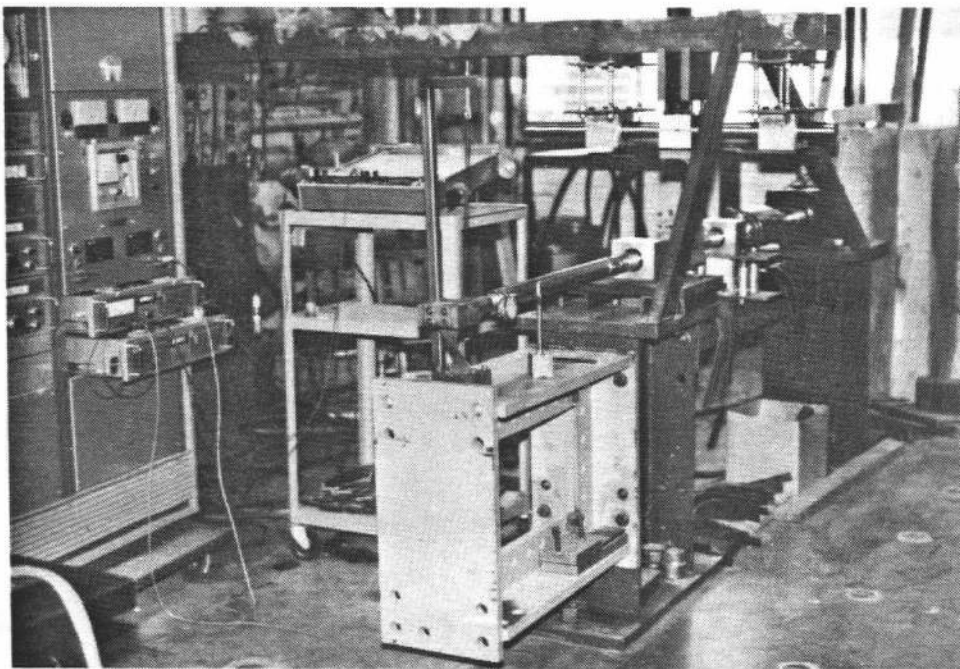


Fig. 3: Test Set-Up Low Cycle Fatigue Tests

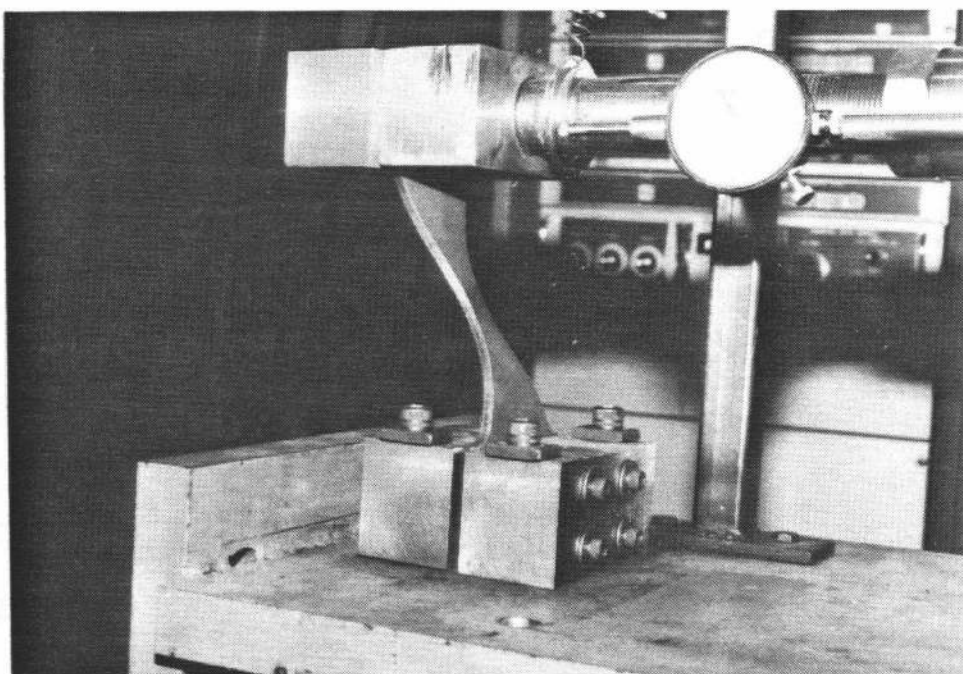


Fig. 4: X-Shaped Energy Absorbers

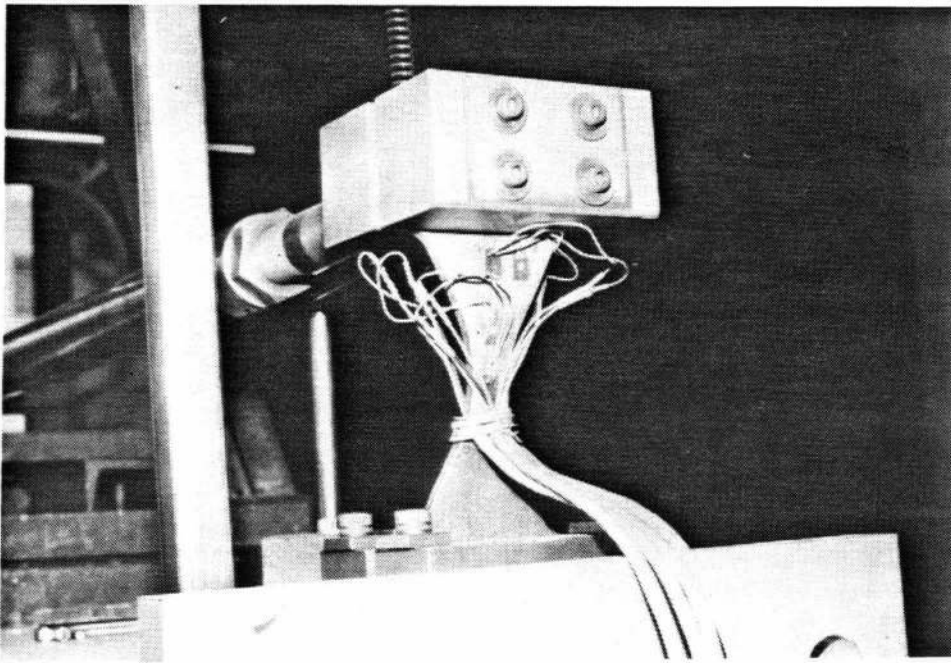


Fig. 5: Strain Gauges Applied to Energy Absorber

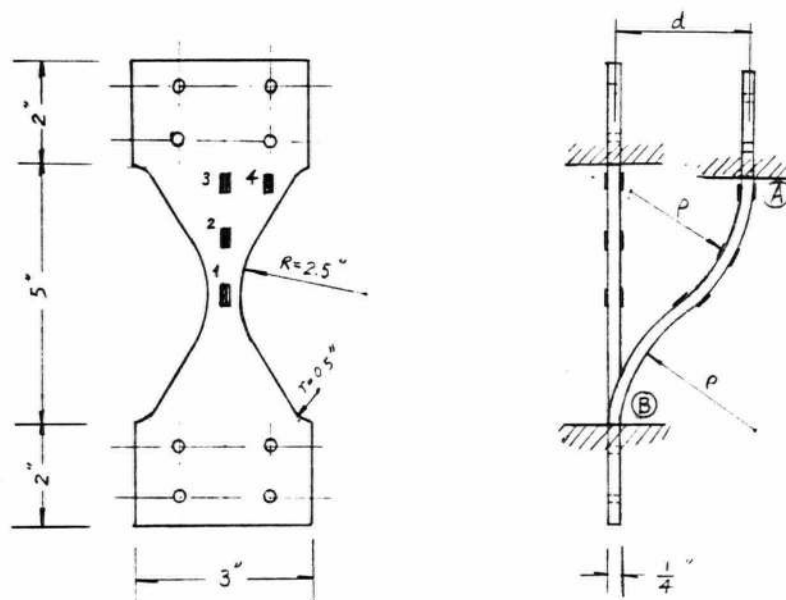


Fig. 6: Locations of Strain Gauges

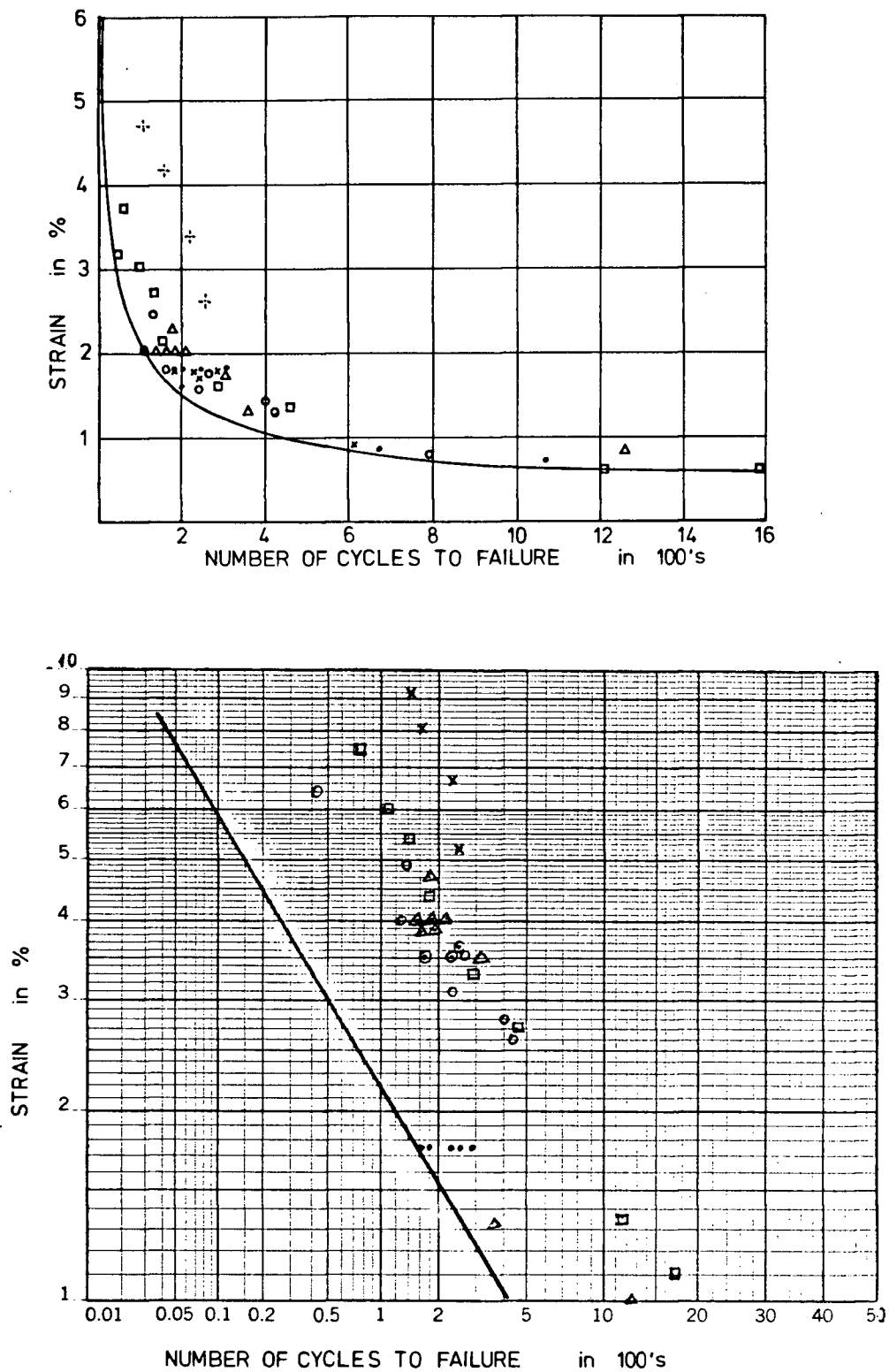


Fig. 7: Test Results of Relation of Strain and Cycle to Failure

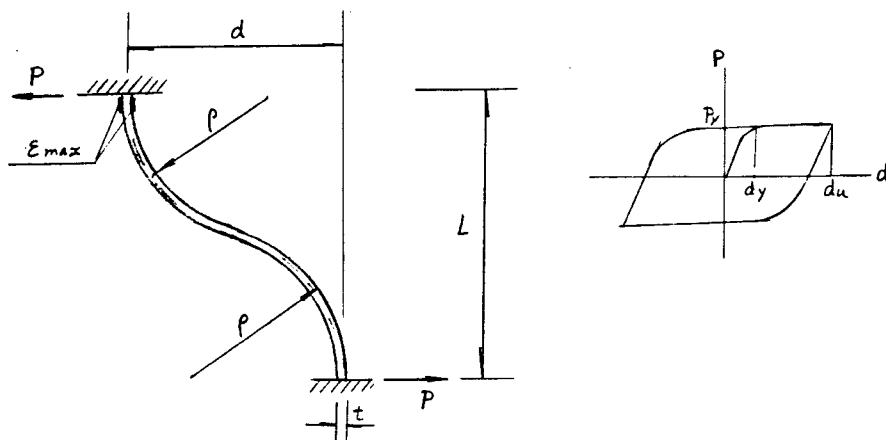


Fig. 8: Characteristic Values and Hysteresis Loop of Energy Absorber, d, L, t, ρ in [INCH], P in [KIPS]

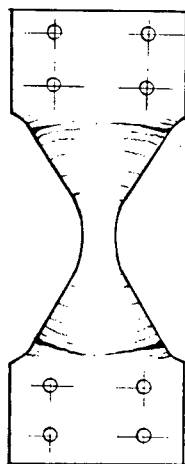


Fig. 9: Microcrack Development in Low Cycle Fatigue Test

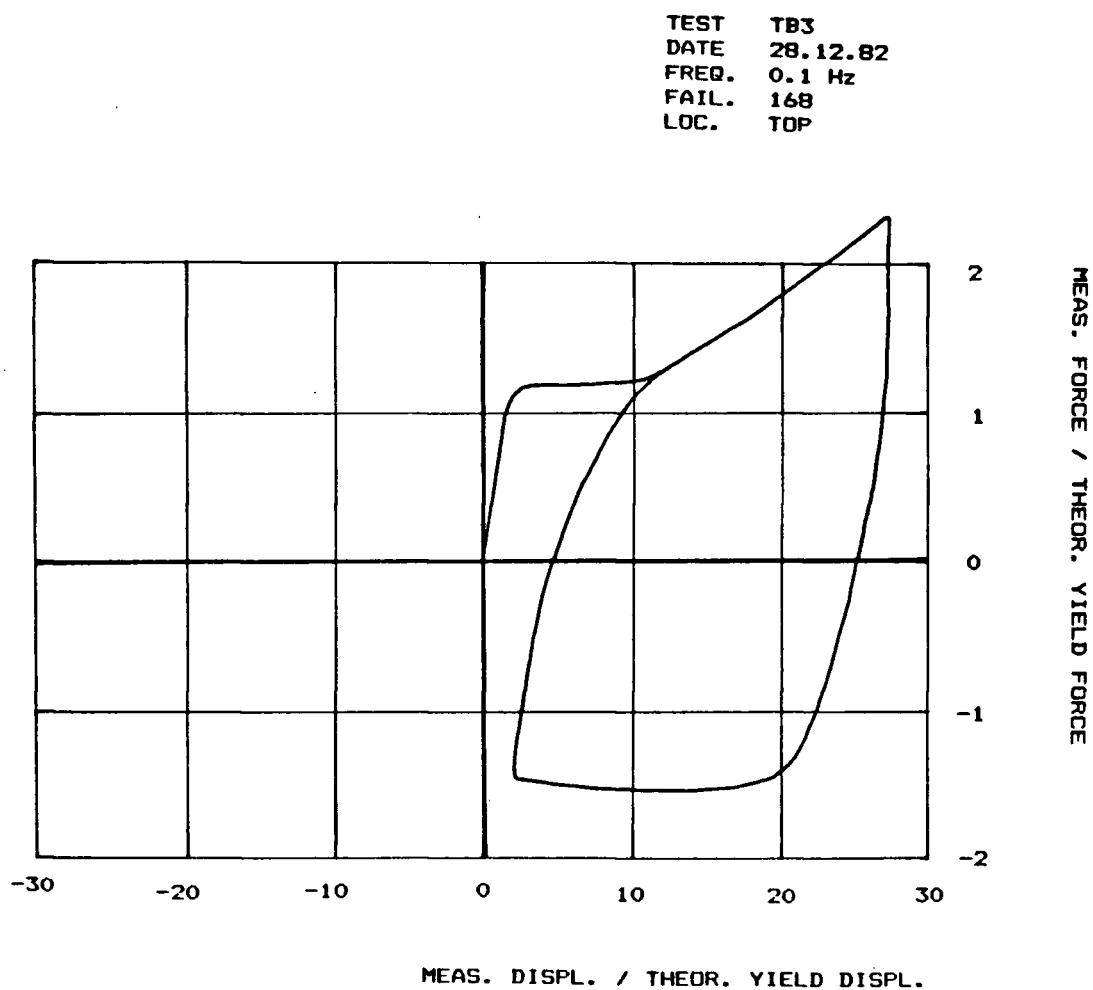


Fig. 10: Hysteresis Loop for Biased Energy Absorber

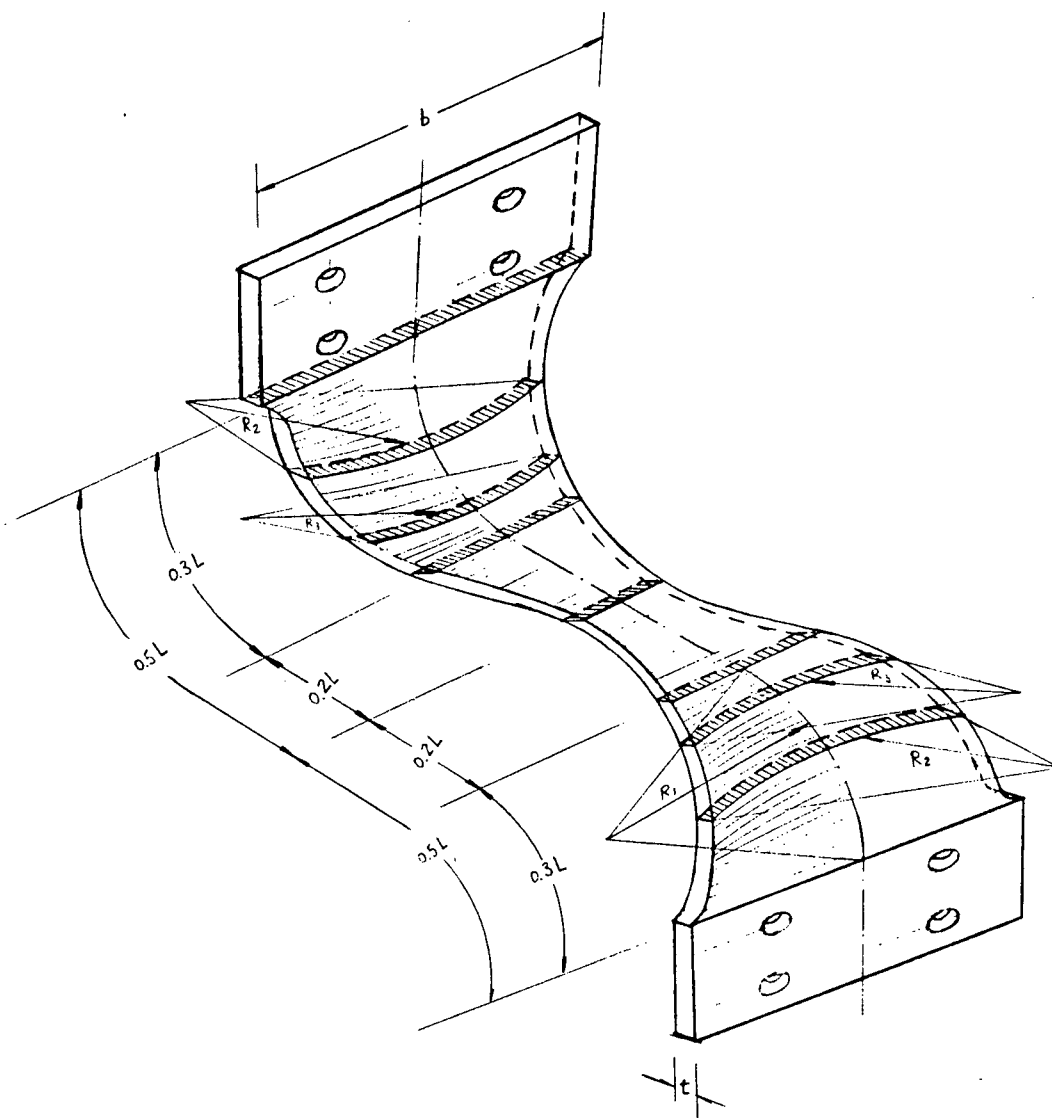


Fig. 11: Anticlastic Bending of Energy Absorber

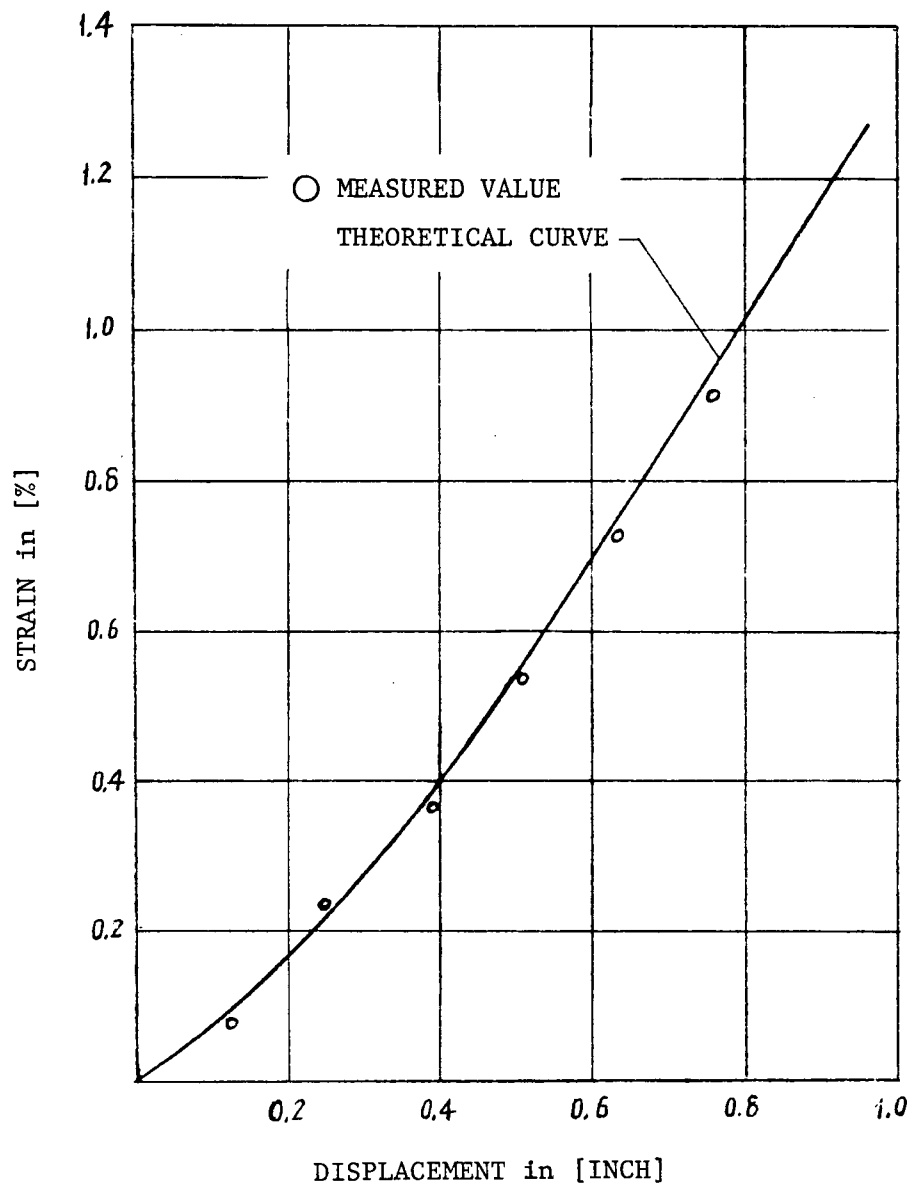


Fig. 12: Strain-Displacement Relation for Energy Absorber

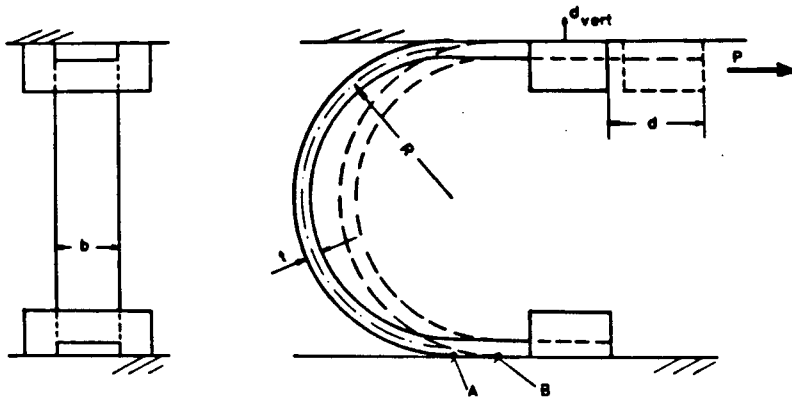


Fig. 13: Quarter Component of Double Yield Ring

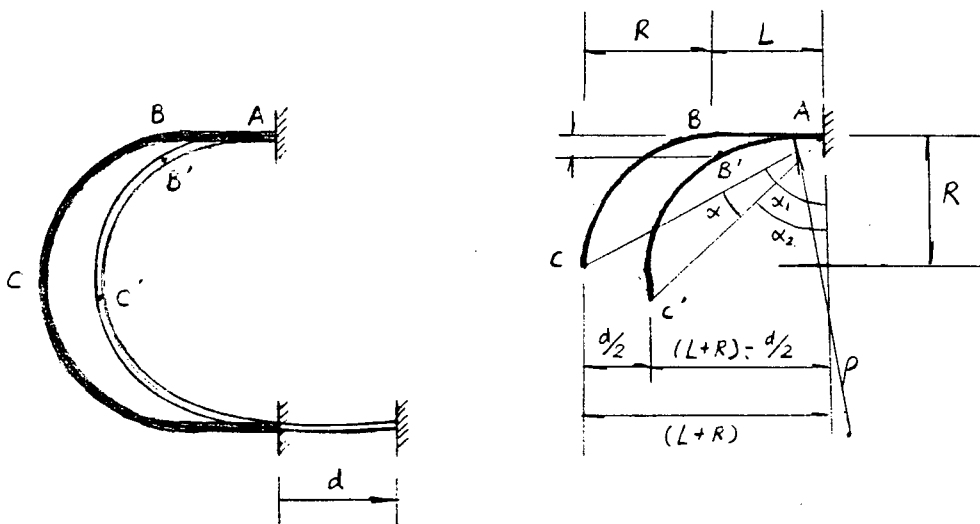


Fig. 14: Geometric Deformation of Yield Ring

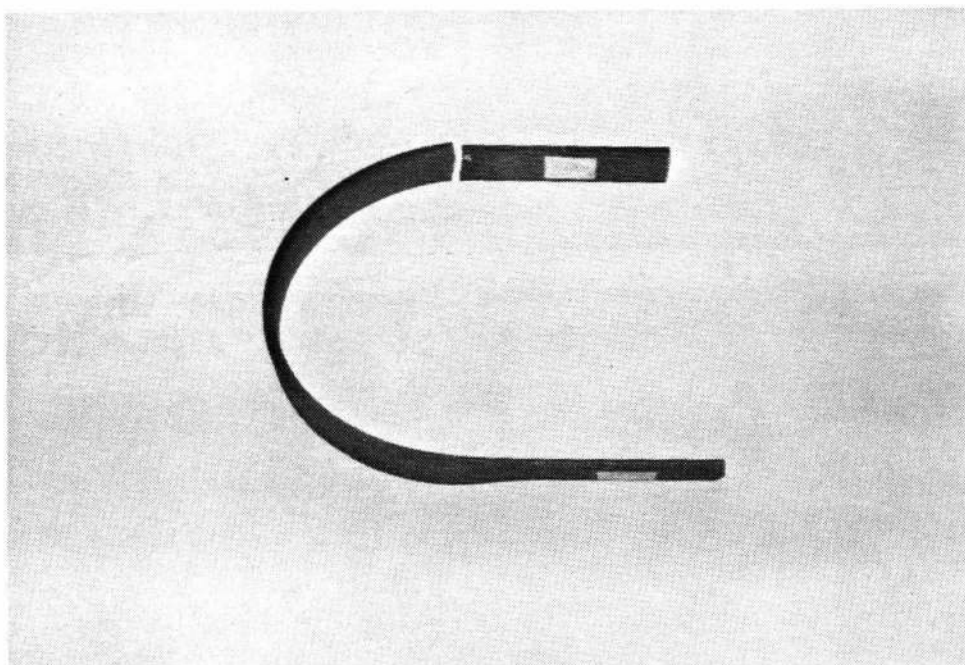


Fig. 15: Fractured Yield Ring

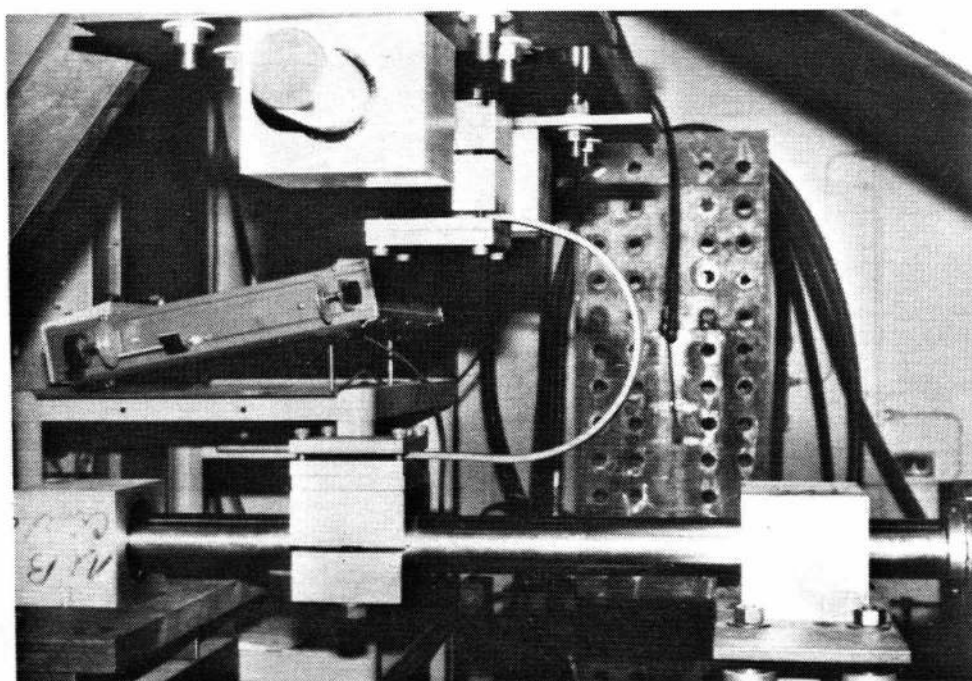


Fig. 16: Displaced Yield Ring

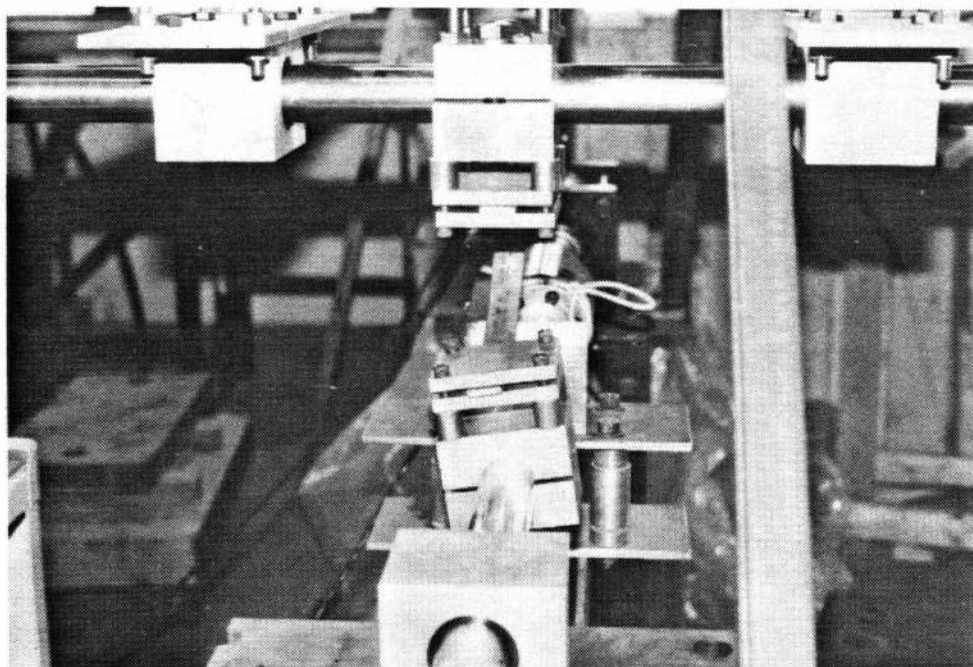


Fig. 17: Twisted Yield Ring

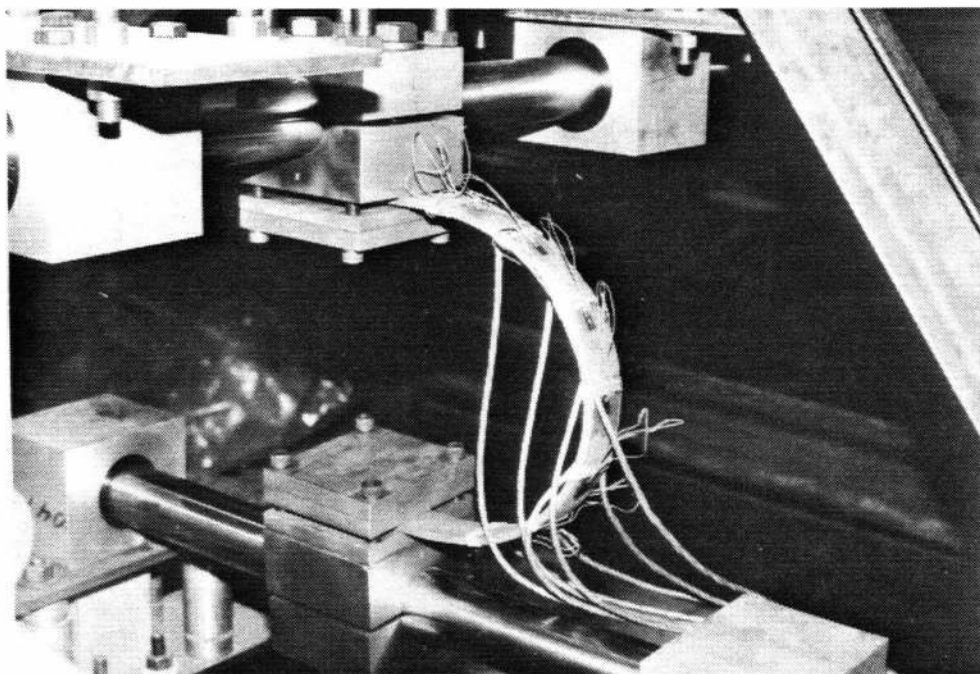


Fig. 18: Yield Ring with Applied Strain Gauges

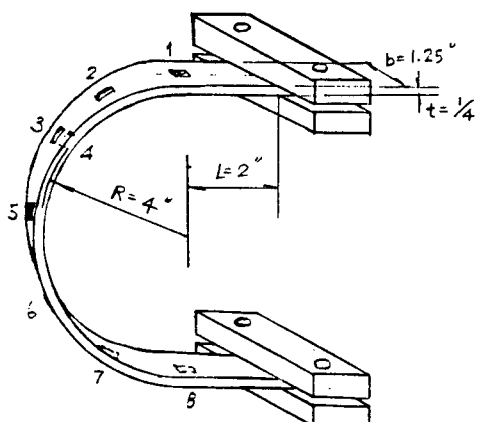


Fig. 19: Locations of Strain Gauges on Yield Ring

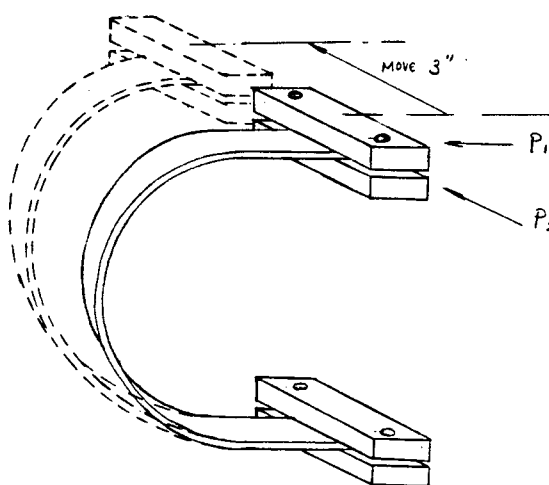


Fig. 20: Displacement of Yield Ring in Y-Direction

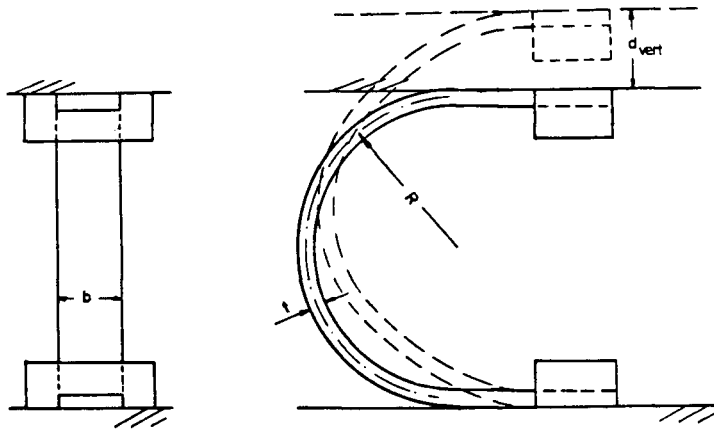


Fig. 21: Displacement of Yield Ring in Z-Direction

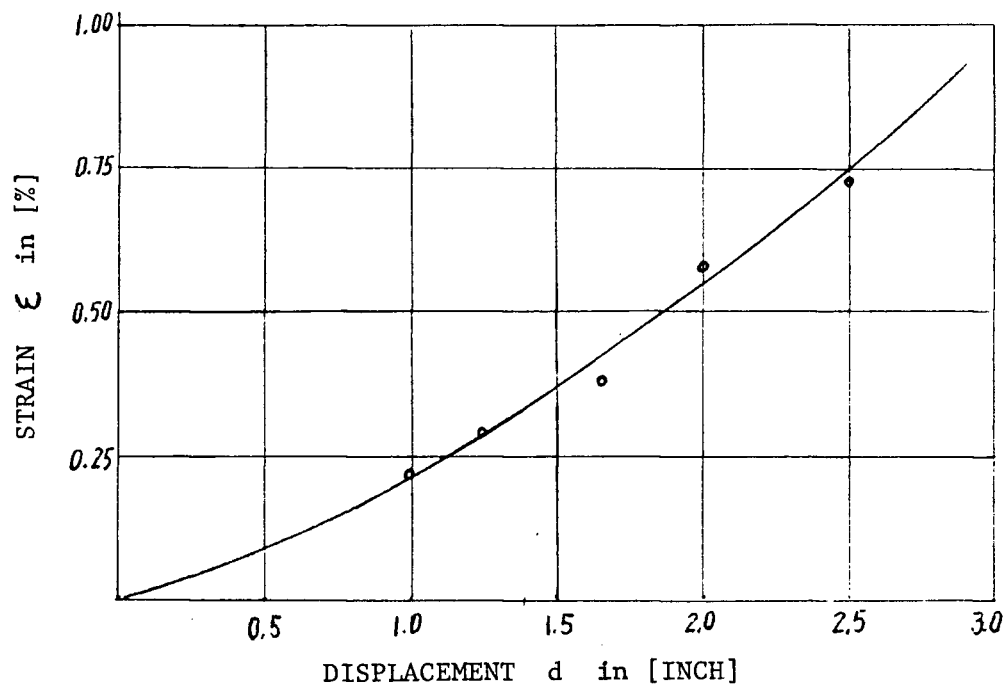


Fig. 22: Strain-Displacement Relation of Yield Ring

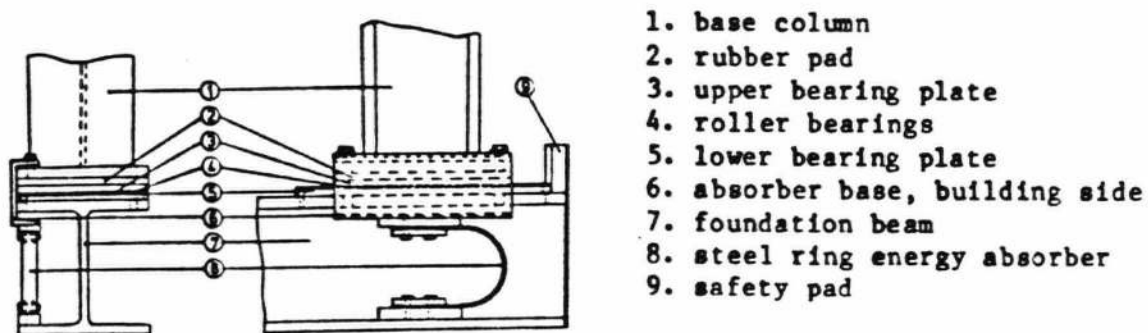


Fig. 23: Components of Base Isolation Model [7]

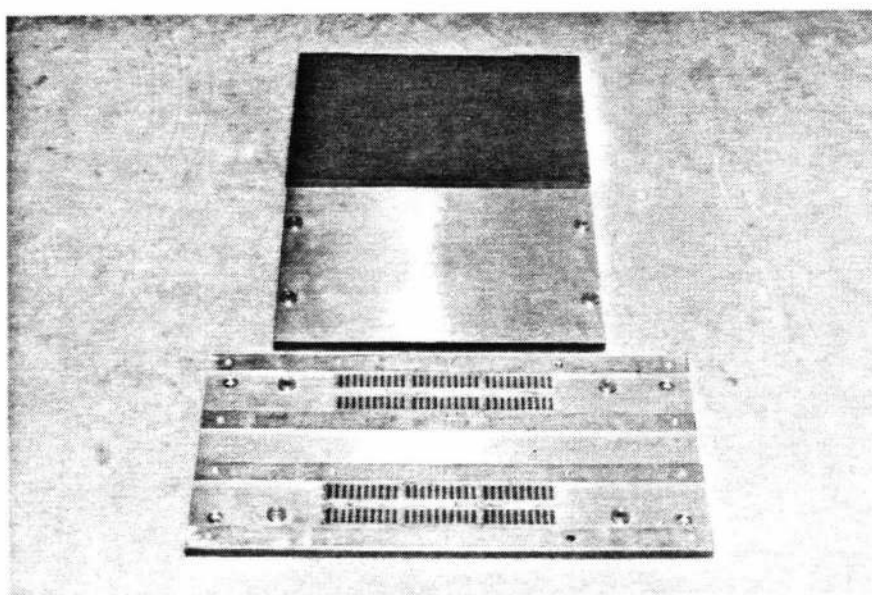


Fig. 24: Roller Element [18]

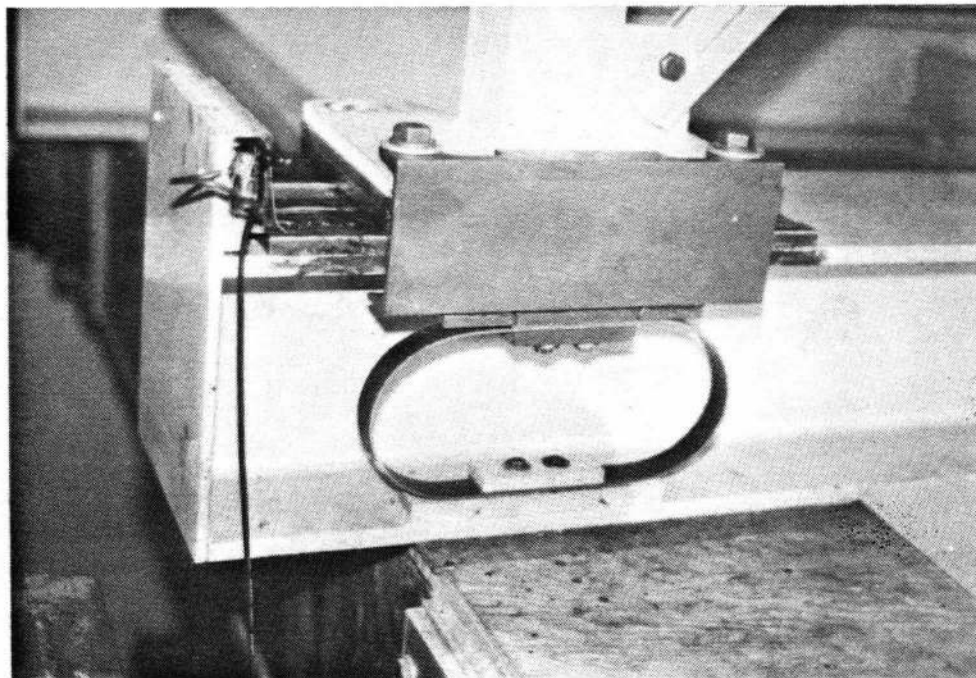


Fig. 25: Base-Isolation System With Two Quarter Yield Rings

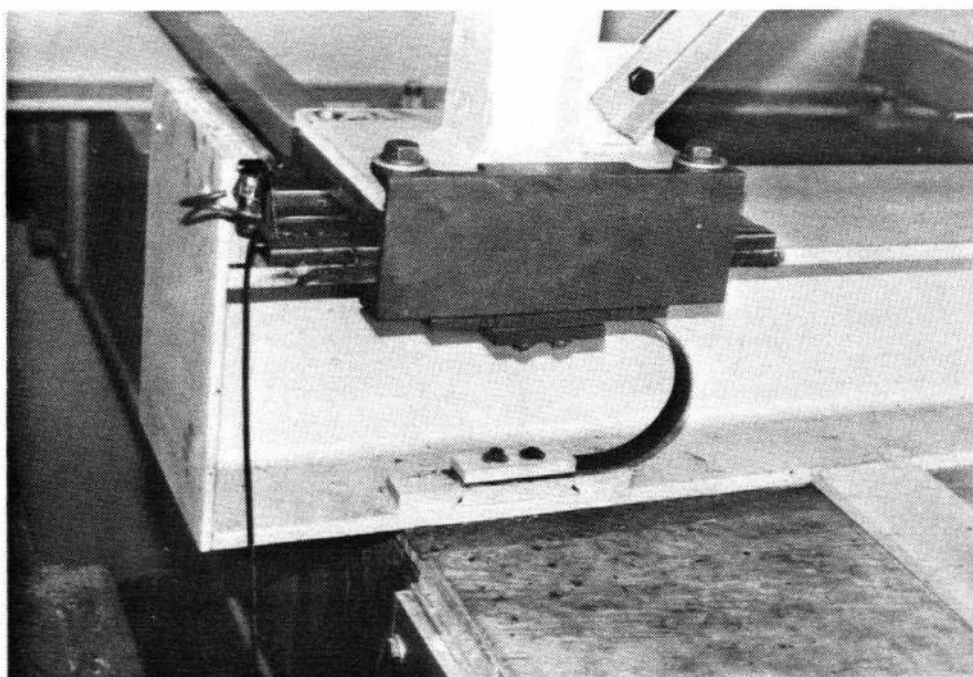


Fig. 26: Base-Isolation System With One Quarter Yield Ring

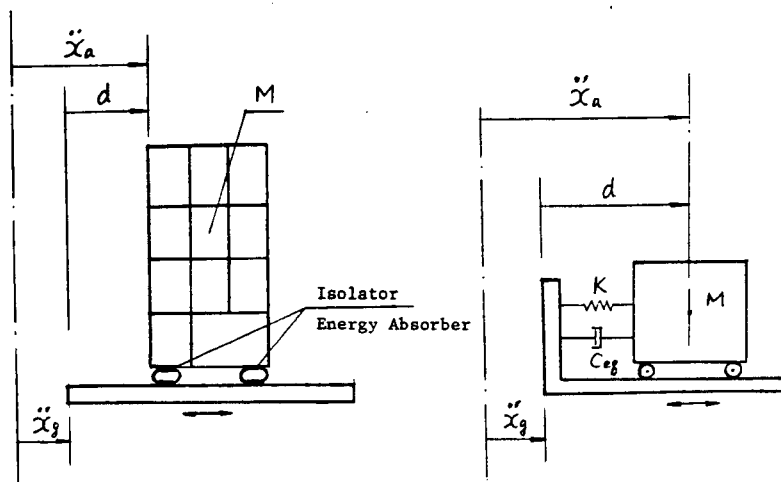


Fig. 27: Structure and Model With Base-Isolation and Yield Ring

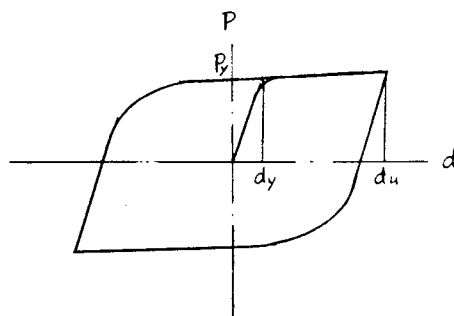


Fig. 28: Load Displacement Hysteresis Loop for Yield Ring

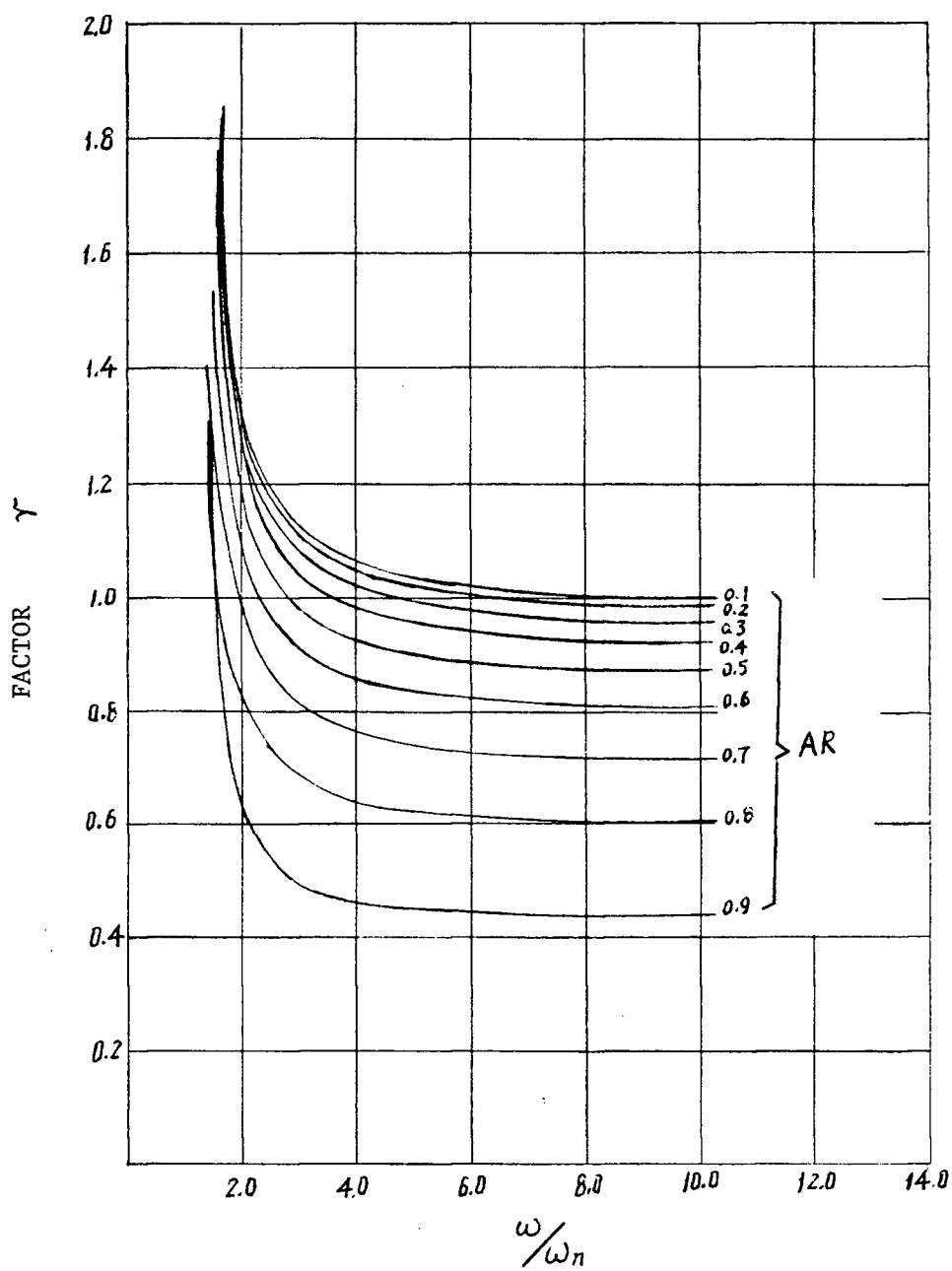


Fig. 29: Displacement Magnification Factor for Different Attenuation Ratios

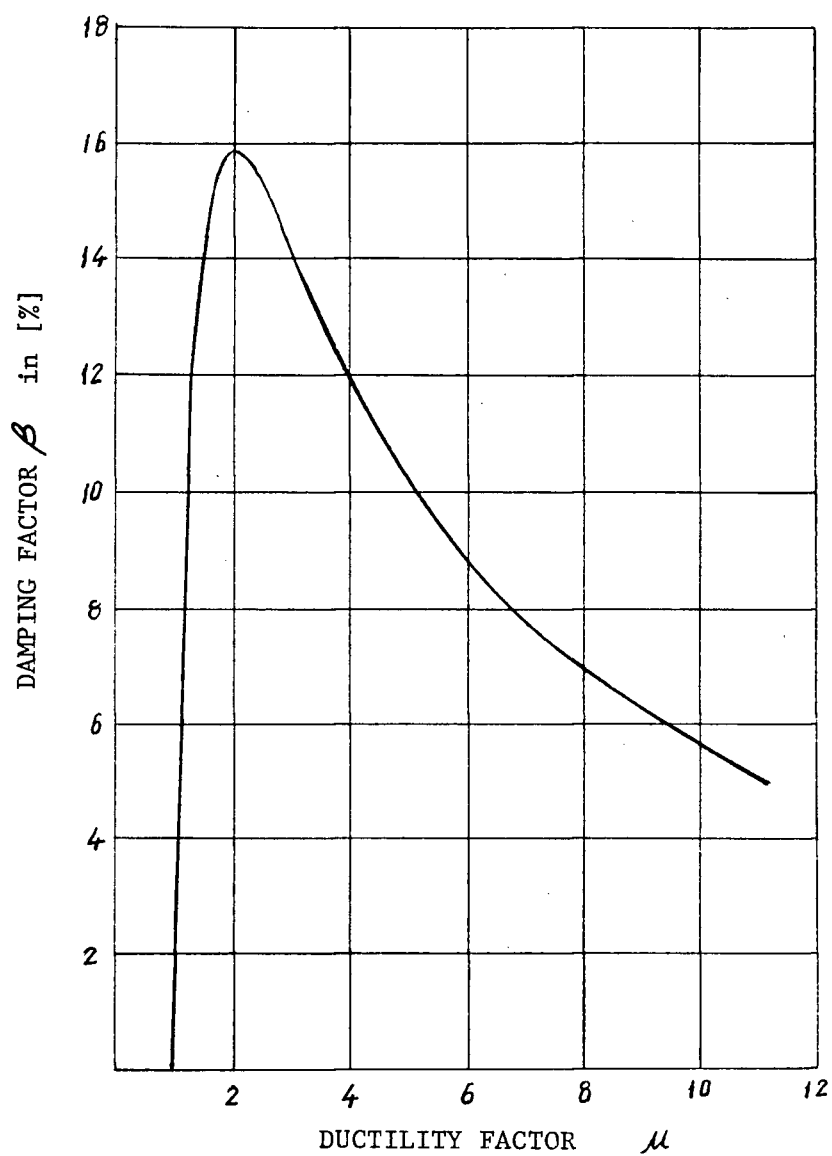


Fig. 30: Relation of Damping and Ductility Factor

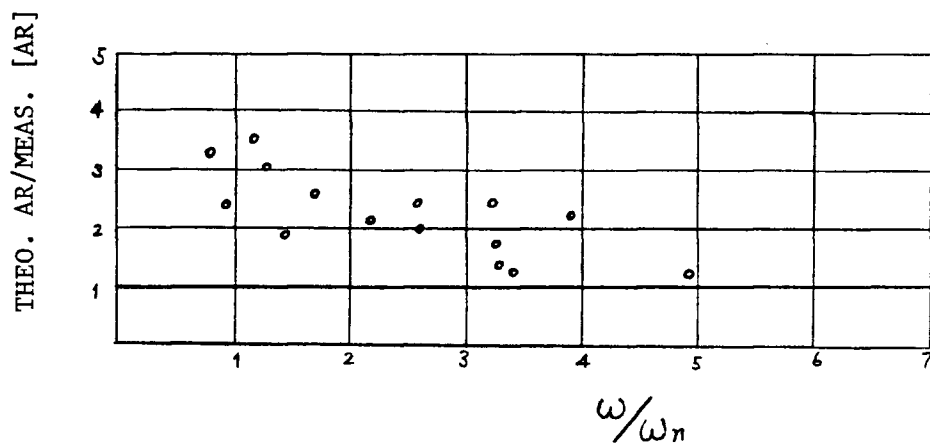


Fig. 31: Attenuation Ratio Over Frequency Ratio for Sinusoidal Excitation

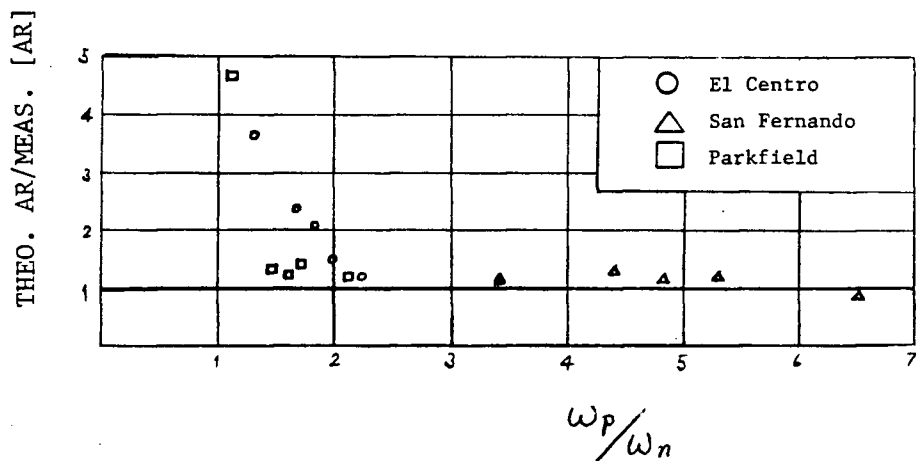


Fig. 32: Attenuation Ratio Over Frequency Ratio for Earthquake Excitation

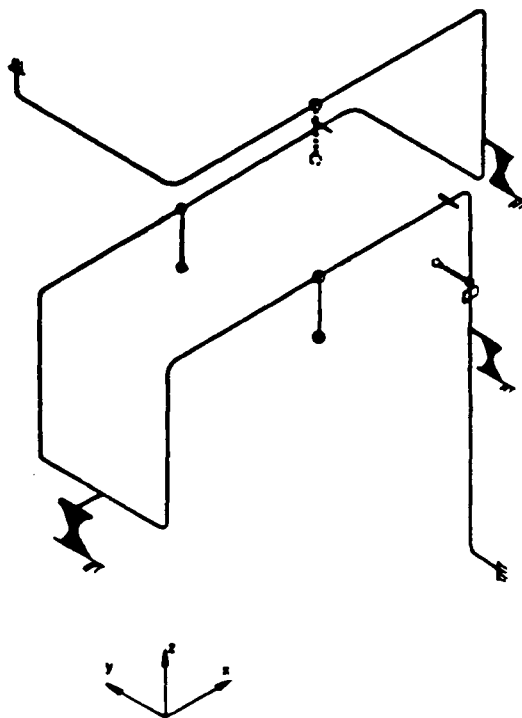


Fig. 33: X-Shaped Energy Absorber Implemented in Flexible Spatial Piping System, Schematic from [4]

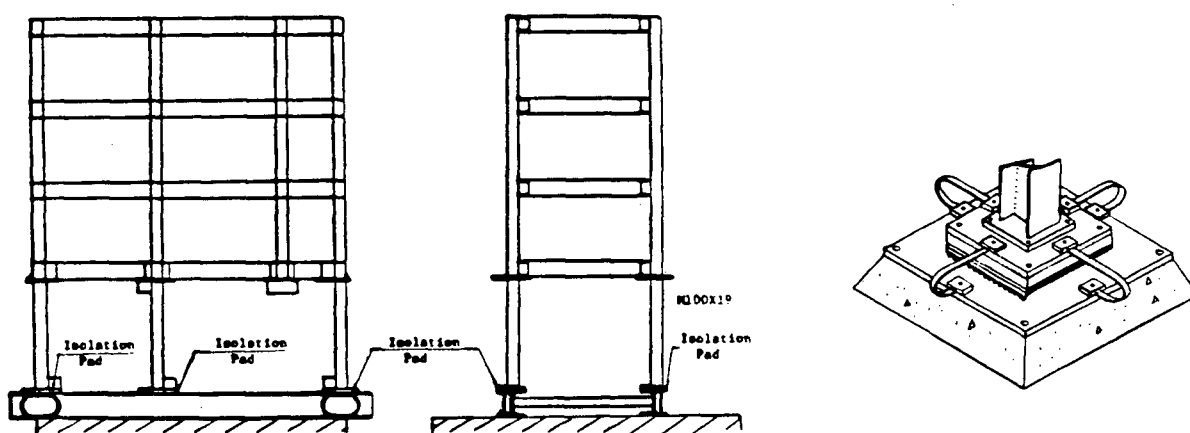


Fig. 34: Yield Rings Implemented in Base Isolation System, From [7], Insert: Proposal for Bi-Directional Use [18]